Chapter 4

Ocean near-surface layers

Baylor Fox-Kemper[a], Leah Johnson[a] and Fangli Qiao[b]

[a]*Brown University, Department of Earth, Environmental, and Planetary Sciences, Providence, RI, United States,* [b]*First Institute of Oceanography, Ministry of Natural Resources, Qingdao, China*

4.1   Introduction

The most energy-dense turbulence in the ocean occurs in the upper boundary layer. This turbulence is driven by winds, waves, and buoyancy forcing, and its fate may be viscous dissipation, the creation of potential energy through mixing and entrainment, or energy loss through downward propagating internal waves. Typically all fates occur to some degree.

Fig. 4.1 shows an example budget of turbulent processes leading to dissipation of mesoscale kinetic energy in a global high-resolution (nominal 0.1°) model (Pearson et al., 2017). Fig. 4.1a shows vertical friction exceeds both horizontal dissipation and bottom drag, and vertical dissipation within the boundary layer is by far the most dissipative parameterisation of kinetic energy. Fig. 4.1b shows this dissipation is highly intermittent and fairly characterised by an approximately log-normal distribution, with the most likely value orders of magnitude higher than typical of turbulence values outside of the boundary layer. Global dissipation of turbulent kinetic energy is estimated to be 1.8 TW (Waterhouse et al., 2014), or 1.3×10^{-9} W kg^{-1} on average. Within the surface mixing layer, values of 1×10^{-5} W kg^{-1} are common.

The fundamental oceanographic notion of water mass formation typically relies upon surface ventilation, i.e., exposure to surface boundary-layer mixing, where waters are transformed by exchanges with the atmosphere, rapid vertical mixing that overcomes stratification, and exposure to radiative forcing. An example of this conceptualisation are the metrics of "ideal age" or transit time, framings that consider aging of water masses that start at zero when exposed to the surface (Hall and Haine, 2002). The only rival mixing processes, in terms of transforming water masses, are when neighbouring water masses sharing similar densities combine (e.g., at the Mediterranean outflow or Southern ocean fronts: Jones and Abernathey, 2019), or when intense bottom overflows entrain (e.g., leading to North Atlantic deep water and Antarctic bottom water: Snow et al., 2015; Yankovsky et al., 2021).

Ocean boundary layers, their atmospheric boundary layer partner, and turbulence within both play an important role in air-sea fluxes (Fig. 4.2). Mathematically, boundary layers are where the ocean boundary conditions are met: stress, heating, and freshwater fluxes are basic ingredients for establishing the surface layer setting, but so too are the pressure matching boundary condition and the surface cohesion of the dynamical boundary condition (or its violent restructuring in the case
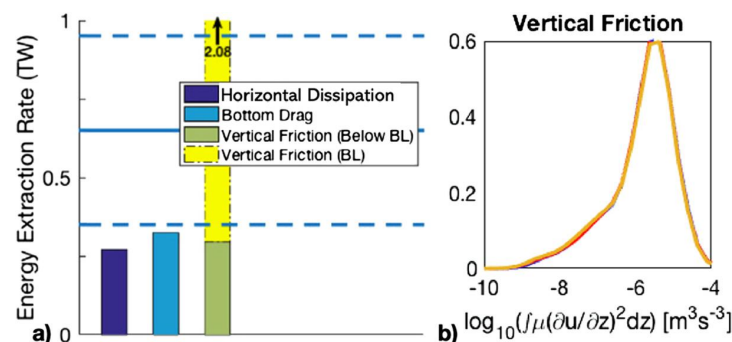

FIGURE 4.1 Global kinetic energy extraction rate by frictional processes in a global mesoscale-resolving simulation. (a) Global integrals of horizontal sub-grid dissipation, bottom drag, and vertical friction within and without the boundary layer. (b) Probability distribution (over horizontal location) of vertically-integrated energy dissipation by vertical friction (overlaid lines show results from three different simulations differing in horizontal dissipation schemes). Redrawn from Pearson et al. (2017).

of spray and bubbles) which are important for waves. On their distal side, they connect to deeper ocean waters and the free atmosphere. Regionally, they connect to the hydrosphere through rivers and the cryosphere (sea ice and ice shelves). There is also an important role for boundary layers in the biosphere: humans and other terrestrial species spend most of our lives in the atmospheric boundary layer, and the light-rich (euphotic) zone of the oceans is essentially collocated with the oceanic boundary layer. As these layers are attached to the atmosphere or cryosphere, it is difficult to disentangle these boundary layers from one another. Indeed, an approach sometimes taken is to denote a "wavy layer," which contains part atmosphere and part ocean (waves, spray, bubbles, foam, etc.), as effectively done in Janssen (2012). In summary, boundary layers mediate exchanges between the spheres.

These layers are active and evolve on a variety of timescales, and we are becoming increasingly aware of the importance of this variability. Particular focus had been on process interaction of vertical or isotropic turbulence with phenomena that occupy larger horizontal dimensions—chiefly at the submesoscale and mesoscale (see Chapters 8 and 9 of this book). The time it takes to mix or convect across the ocean boundary layer is measured in minutes to days, but many important impacts of these layers are manifested by their diurnal and seasonal variability. They are a critical player in the dominant modes of interannual and decadal variability.

Surface layers also play an important role in geochemistry, largely through exchanges of carbon and oxygen. Often, due to the rapid timescales of chemical reactions and stoichiometry in comparison to the relatively slow timescales (minutes to hours) of boundary layer mixing, and the relatively minimal vertical variations of properties within the mixed layer; the mixed layer can be assumed to be chemically homogeneous and relatively quick to arrive at a saturation level of chemical constituents, according to Henry's Law. However, it is possible for the finite timescale of reactions or piston velocity to be rivaled by ocean turbulence mixing timescales, in which case other effects can occur (Smith et al., 2018). Chapter 13 of this book discusses important aspects of the decreasing boundary layer saturation levels of oxygen under global warming. Bubbles and spray may also have interesting physical-chemical effects on gas transfer (e.g., Liang et al., 2013).

The surface layers are critical biologically, as they coexist with the euphotic zone and can govern how the essentials for life are distributed. The *critical depth hypothesis* (Sverdrup, 1953) posits that the spring phytoplankton bloom initiation in the North Atlantic can be understood by the increased light exposure of primary producers within a shoaled mixed layer. Taylor and Ferrari (2011) brought a more dynamical aspect to this theory, referred to the *critical turbulence hypothesis*, which considers the residence time of phytoplankton within the euphotic zone during mixing, and is in line with other elaborate theories linking zooplankton behaviour to mixing. Submesoscale restratification can accelerate the spring bloom, through its effect on suppressing turbulence and shoaling the mixed layer (Mahadevan et al., 2012), a beautiful example of submesoscale-boundary layer interaction with important consequences.

As a final example application of surface layers in real world problems, consider the location, detection, and capture of pollutants, such as oil and plastics. Often pollutants may be more buoyant than seawater, allowing them to rise through the boundary layer to the surface and accumulate where surface convergences lie (Taylor, 2018; D'Asaro et al., 2018). Alternatively, pollutants may gather, clump, flocculate, grow colonies, or be damaged to become negatively buoyant (Taylor et al., 2020). In both cases, the buoyancy of the pollutants can affect the dynamics as bubbles and spray do, or at the least (if pollutant concentrations are low) may be sorted into particular dynamical features, which influence their collection (e.g., van Sebille et al., 2020), detection (e.g., Brunner et al., 2015), and mitigation (e.g., Choy et al., 2019). Surface convergences and vertical velocities are intimately linked by the continuity equation, and surface convergences strongly affect the observation of boundary layer turbulence statistics of floats and drifters that accumulate much as pollution does (Chang et al., 2019; Pearson et al., 2019, 2020).

There are a number of recent review and broad perspective papers on the ocean surface layers (Umlauf and Burchard, 2005; Sullivan and McWilliams, 2010; Belcher et al., 2012; D'Asaro, 2014; Li et al., 2019) and waves (Cavaleri et al., 2012), as well as excellent treatment of key concepts in textbooks and monographs (Thorpe, 2007; Wyngaard, 2010; Csanady, 2000; Baumert et al., 2005). This chapter will therefore touch on basic theory (Section 4.2), but highlight recent developments in observations (Section 4.3), modelling (Section 4.4), and global perspectives (Section 4.5) emphasising processes, tools, and recent discoveries that are less well understood and do not appear commonly in textbooks.

4.2 Mixing layers and mixed layers in theory

Fig. 4.2 schematises the ocean surface layers. The atmospheric boundary layer (here idealised as a neutral (no stratification stable or unstable) boundary layer with a capping inversion), ocean mixing layer, ocean mixed layer ($0 > z > -h$, where temperature and salinity stratification is small), and the (assumed-stably) stratified thermocline and halocline that make up the upper pycnocline are illustrated. Solar radiation is noted to penetrate exponentially over roughly the mixed layer depth (depending on water clarity). Longwave (infrared, blackbody) radiation and turbulent fluxes of energy (latent, associated
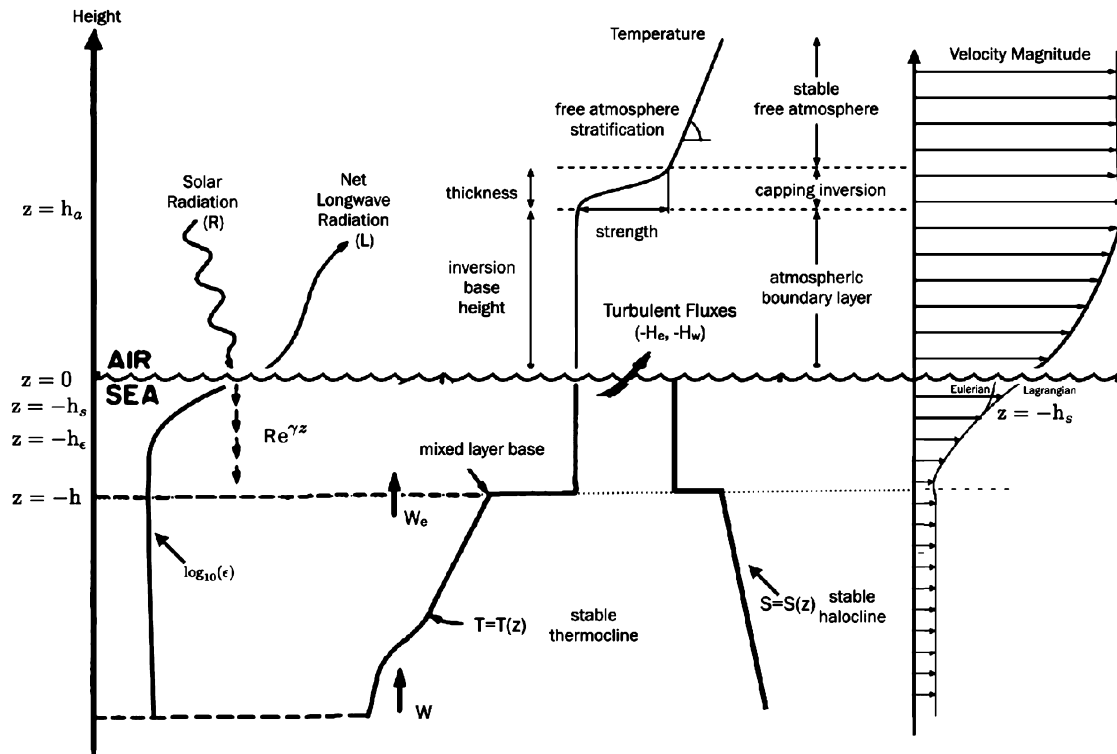
FIGURE 4.2 Schematic of the ocean surface layers, including entrainment velocity w_e, upwelling w, temperature T, salinity S, turbulent fluxes of thermal energy H_e, and freshwater H_w, dissipation ϵ, Stokes depth h_s, mixing-layer depth h_ϵ, and mixed-layer depth h.

with evaporation/precipitation, and sensible, associated with warm/cold air and water) can be totalled for air-sea energy exchanges that are realised within centimetres of the surface. Turbulent and radiative fluxes within the ocean and atmosphere tend to continue to the capping inversion and mixed layer base and beyond (during strong convective or shear forcing).

Waves present on the air-sea interface extend into the ocean ($0 > z > -h_s$), and are part of the exchanges and links between atmospheric (e.g., Suzuki et al., 2011) and oceanic (e.g. Teixeira and Belcher, 2002) turbulence. The ocean velocity profile on the right of Fig. 4.2 notes the difference between the Eulerian velocity (i.e., the velocity profile averaged over a wave period at a point in space, thus not including wave orbital velocities) and the Lagrangian velocity (the velocity averaged over a wave period following the path of the wave and current motion). As wave orbits carry parcels closer to the surface where the wave motion is faster; and then away from the surface, where it is slower, the Eulerian and Lagrangian velocities are not equal. This difference is the Stokes drift velocity, which decays rapidly away from the surface (depending on the wavelength of the waves, Webb and Fox-Kemper, 2011, as simplified in Fig. 4.2 by a single depth h_s). The waves shown here are not sinusoidal, which schematises the non-linear sharpening and breaking that occur from wave dynamics or whitecapping that would be expected under windy conditions.

The ocean mixing layer is the layer of active turbulence ($0 > z > -h_\epsilon$), where energy flow into turbulence and turbulence dissipation is elevated. When measurements or simulations of the dissipation rate of turbulence (ϵ) are available, this layer can be defined as the surface layer over which the value exceeds a typical background. The exceedance is typically many orders of magnitude above the background level in the mixing layer, which the schematic notes by showing a fast decay in $\log_{10}(\epsilon)$. Alternatively, the mixing layer can be defined based on the turbulent energy production or fluxes.

The mixed layer ($0 > z > -h$) may be deeper than the mixing layer during periods of relative calm after a deep mixing event. Alternatively, the mixing layer might be deeper than the mixed layer during active mixing and entrainment of stratified water into the mixed layer. Thus the mixed layer evolves semi-independently of the turbulence, lagging behind the active forcing to record a history of past forcing and restratification (the set of processes by which stratification, especially density stratification, is recovered after mixing). There are a variety of restratification processes, but the most important are solar (stronger heating near the surface) and dynamical (collectively processes—e.g., eddies, fronts, plumes, instabilities,

filaments, geostrophic adjustment—that extract potential energy from the low to unstable stratification of the mixed layer by sorting light anomalies toward the surface and dense anomalies to depth).

The mixed layer base during convection or mixed layer deepening is punctured intermittently by plumes and jets of mixed layer water. The transition zone or entrainment layer, where this occurs, is partly diabatic, while the thermocline, halocline, and pycnocline below are subject to much lower levels of diabatic mixing. Some care is needed in defining this transition layer in practice, in a way that depends on scale: on small scales turbulence and diabatic entrainment determine the layer (Johnston and Rudnick, 2009; Li and Fox-Kemper, 2017, 2020); at submesoscales intrusions, ramps, and intra-thermocline eddies; and at mesoscales by isopycnal heaving and outcrops from eddies and fronts. The surface layer turbulence importantly responds and couples to the structures of eddies and fronts displacing the mixed layer base (Smith et al., 2018; Taylor, 2018; Taylor et al., 2020), and on large-scale average, such as used in climate models, diabatic and adiabatic processes are blended together in a general "transition zone" (Danabasoglu et al., 2008).

The atmospheric literature uses slightly different terminology (Holtslag and Nieuwstadt, 1986; Wyngaard, 2010). There is a surface layer, a mixed or upper layer, and then an entrainment or interfacial layer, where there might be a capping inversion. The mixed layer has similar meaning in both fluids, but the surface layer corresponds more directly to what is called the log-layer in the ocean, rather than the mixing layer. There does not appear to be a common use of a conceptual distinction between the mixing layer based on turbulent dissipation and the mixed layer in the atmosphere, even when dissipation is directly measured (e.g., Muñoz-Esparza et al., 2018). This may have to do with the rapid nightly restratification that keeps these two atmospheric layers tracking closely together.

In addition to vertical gradients, the surface layers also vary horizontally. Sometimes there is a strong dynamical coupling of these lateral gradients and the vertical structure of the surface layers, such as during submesoscale restratification or frontal slumping. These lateral gradients affect lateral transport, restratification, and air-sea fluxes. They are not the emphasis of this chapter, but are the focus of Chapters 8 and 9 of this book. Nonetheless, significant recent work has explored the relationships between lateral gradients and the surface layers, and these relationships will be discussed here.

4.2.1   Mixing and surface layers: Monin–Obukhov scaling

Monin and Obukhov (1954) proposed a scaling theory and similarity solutions for a dry atmospheric boundary layer over an infinite, rough surface, neglecting horizontal heterogeneities, but including heat fluxes through the surface, which distinguishes this theory from the earlier logarithmic "law of the wall" turbulent boundary layer (Von Kármán, 1930). Given the dynamical similarity of the dry atmosphere situation to an oceanic boundary layer, this same approach is often converted to an infinite, oceanic boundary layer under a rigid surface with cooling or heating applied at this surface. Here we will consider some aspects of coupling an M–O ocean underneath an M–O atmosphere.

4.2.1.1   Monin–Obukhov scaling

For simplicity, we will consider both the atmospheric and oceanic boundary layers to be Boussinesq fluids, with a background atmospheric density $\rho_a \approx 1.225$ kg m^{-3} and oceanic density $\rho_o \approx 1025$ kg m^{-3}, taking typical sea level values. This assumption oversimplifies the energy cycle slightly (see Section 4.2.2.3) and has implications for the relationships between salinity and freshwater fluxes (Nurser and Griffies, 2019).

The atmosphere and ocean are connected by an exchange of momentum (stress, τ) and thermal energy. In addition to the air-sea exchange of thermal energy ($Q_{as} = Q_L + Q_S$, positive for ocean warming and composed of latent and sensible components), there is also short-wave and long-wave radiation (R+L, positive for surface warming), which for the purposes of the M–O theory, can be considered to penetrate air without absorption in the boundary layer and penetrate seawater not at all. Reflections, albedo, and a balance between downwelling and upwelling longwave radiation is assumed, so that R+L represent only the energy transferred not the raw insolation or blackbody formulas. The total heating of the ocean applied at the surface in the M–O theory is thus $Q_{net} = R + L + Q_L + Q_S$, whereas the total heating of the atmosphere from the surface is $-Q_L - Q_S$ (assuming negligible net direct radiative heating or cooling of the atmosphere within the boundary layer).

M–O theory is normally framed in terms of a surface friction velocity scale, formed from the stress and used to scale the energy forcing at the surface and turbulent velocities within the boundary layer. To address both fluids, two velocities are needed, which we'll denote with subscript o for ocean and a for atmosphere as for the densities. Within the surface layers, these velocity scales are proportional to the turbulent velocities, and from this knowledge the profiles of mean velocity can be found.

The friction velocities are found from the surface stress,

$$\rho_o u_{*o}^2 = |\boldsymbol{\tau}| = \rho_a u_{*a}^2. \tag{4.1}$$

In the absence of other vector quantities, Galilean invariance suggests that parameterisations of the vector stress should be oriented along the air-sea velocity difference. Taking the traditional sign convention of the stress exerted by the winds on the surface,

$$-\rho_o \overline{\mathbf{v}'_o w'_o}^{0^-} = \rho_o u_{*o}^2 \frac{\overline{\mathbf{v}}_a - \overline{\mathbf{v}}_o}{|\overline{\mathbf{v}}_a - \overline{\mathbf{v}}_o|} = \boldsymbol{\tau} = \rho_a u_{*a}^2 \frac{\overline{\mathbf{v}}_a - \overline{\mathbf{v}}_o}{|\overline{\mathbf{v}}_a - \overline{\mathbf{v}}_o|} = -\rho_a \overline{\mathbf{v}'_a w'_a}^{0^+} , \tag{4.2}$$

where $\mathbf{v}$ indicates the *horizontal* velocity and w the vertical velocity component (later $\mathbf{u}$ will indicate 3D velocity, i.e., $\mathbf{u} = \mathbf{v} + w\hat{\mathbf{z}}$). The primes denote deviations from the horizontal mean, and the overbar denotes a horizontal mean. The superscript 0^+ and 0^- indicate that this condition holds in the limit as the surface is approached from above and below, respectively, but does not apply in a thin layer near the surface, which is taken to be a frictional sublayer with specified roughness in the standard M–O theory. The consequences of relative velocities, rather than neglecting the ocean velocity, can be large on mesoscales and submesoscales (Renault et al., 2016, 2018; Chassignet et al., 2020). Both of these assumptions are not as clear of a choice in the presence of waves as will be discussed below.

The M–O depth is a key parameter of the theory. In its most basic form, it is

$$L = \frac{1}{\kappa} \frac{-u_*^3}{\overline{w'b'}^0} = \frac{1}{\kappa} \frac{u_*^2}{b_*}, \tag{4.3}$$

where $\kappa = 0.4$ is the von Karman constant and b is the buoyancy of the fluid in question, which in the M–O theory depends only on the potential virtual temperature: atmosphere ($b = g(T_a - T_r)/T_r$) or ocean ($b = g\beta_T(T_o - T_r)$), with subscript r indicating reference values, such as the mixed layer average temperature. The flux buoyancy b_* is just a convenient scale formed from the buoyancy flux divided by $-u_*$; below we will relate it to surface heat and freshwater fluxes. Following Monin and Obukhov (1954), $L_a < 0$ is taken to indicate convective conditions in the atmosphere and $L_a > 0$ to indicate shear turbulence in a stable stratification. With L defined as above, $L_o > 0$ is convective in the ocean, whereas $L_o < 0$ occurs during restratification (following Reichl and Hallberg, 2018). In both the atmosphere and ocean, $z/L < 0$ indicates convective boundary forcing, and $z/L > 0$ indicates stabilising boundary forcing.

The basic interpretation of the M–O theory is that close to the surface, when $|z/L| \ll 1$, the buoyant forces and buoyant production of energy (scaled by $\overline{w'b'}^0$) are very small in comparison to the shear forces and production ($\overline{\mathbf{v}'w'}\partial\overline{\mathbf{v}}/\partial z$), which lead to the a near-surface that behaves as though all tracers are passive, just as in a neutral boundary layer, where $z/L = 0$. This assumption leads to scaling laws (Section 4.2.2.4) and similarity solutions for this surface layer that depend only on the surface fluxes and distance from the boundary in units of z/L. Recent work has begun to examine how well these ideas extend to more general circumstances and attach to other aspects of the air-sea near-surface layers.

4.2.1.2 Consistent drag laws

M–O theory is often combined with simple scalings for the fluxes between air and sea (Liu et al., 1979; Large and Pond, 1981, 1982; Fairall et al., 1996), although in principle these are independent parameterisations aside from the scaling theory (Monin and Obukhov, 1954). The basic form of these parameterisations is useful to consider here, although more advanced forms are widely considered (e.g., Fairall et al., 1996; Cronin et al., 2019).

$$\boldsymbol{\tau} = -\rho_o \overline{\mathbf{v}'_o w'_o}^{0^-} = -\rho_a \overline{\mathbf{v}'_a w'_a}^{0^+} = \rho_a c_d |\overline{\mathbf{v}}_a - \overline{\mathbf{v}}_o|(\overline{\mathbf{v}}_a - \overline{\mathbf{v}}_o) \tag{4.4}$$

$$|\boldsymbol{\tau}| = \rho_o u_{*o}^2 = \rho_a u_{*a}^2$$

$$Q_S = -\rho_o c_{po} \overline{w'_o T'_o}^{0^-} = -\rho_a c_{pa} \overline{w'_a T'_a}^{0^+} = \rho_a c_{pa} \sqrt{c_d} \sqrt{c_T} |\overline{\mathbf{v}}_a - \overline{\mathbf{v}}_o| \left(\overline{T_a}^{0^+} - \overline{T_o}^{0^-} \right) \tag{4.5}$$

$$= \rho_o c_{po} u_{*o} T_{*o} = \rho_a c_{pa} u_{*a} T_{*a}$$

$$Q_L = \rho_o L_e \overline{w'_o S'_o}^{0^-} /1000 = -\rho_a L_e \overline{w'_a q'_a}^{0^+} = \rho_a L_e \sqrt{c_d} \sqrt{c_q} |\overline{\mathbf{v}}_a - \overline{\mathbf{v}}_o| \left(\overline{q_a}^{0^+} - q_s \right) \tag{4.6}$$

$$= -\rho_o L_e u_{*o} S_{*o}/1000 = \rho_a L_e u_{*a} q_{*a}$$

The water vapour mass mixing ratio q underlies the turbulent flux of freshwater away from the surface. The interfacial value of the water vapour mixing ratio q_s is computed from the saturation mixing ratio corresponding to the sea surface temperature and a small correction due to salinity.

The factor of 1000 in the latent heat flux formula results from the practice of reporting salinity in parts per thousand (‰), rather than in mass fraction. The important balance in (4.6) is that in a coordinate system relative to the surface (i.e.,

sea level pressure), representing freshwater removed through the surface as a turbulent freshwater flux requires a downward salt flux of the same mass (Nurser and Griffies, 2019).

The new M–O flux parameters—T_{*a}, T_{*o}, q_{*a}, S_{*o}—like b_* are simply the surface limit of the turbulent fluxes divided by $-u_{*a}$ or $-u_{*o}$. The specific heat capacities at constant pressure are $c_{po} \approx 3986$ J kg^{-1} K^{-1} and $c_{pa} \approx 1000$ J kg^{-1} K^{-1}, whereas the latent heat of vaporisation is $L_e \approx 2.5 \times 10^6$ J kg^{-1}. The transfer coefficients c_d, c_T, c_q are in fact functions of the reference height, from which the atmospheric velocities are taken, scaled by L_a (Fairall et al., 1996), so these vary depending on the local value of the fluxes through L_a. In data-driven ocean model comparisons (Tsujino et al., 2020; Chassignet et al., 2020), calculating these bulk fluxes from observed atmospheric states is an important part of forcing models (Large and Yeager, 2004, 2009).

4.2.2 Near-surface distinctions from M–O theory and each other

While the M–O similarity theory is a fundamental grounding for basic relationships in the atmospheric and oceanic near-surface layers, and especially the relationships between turbulent velocity scales and boundary forcing, it is insufficient to describe many aspects of interest in these layers. In this section, the deviations from M–O theory are highlighted.

4.2.2.1 Salinity and humidity

Latent heating (i.e., evaporation) affects atmospheric moisture and oceanic salinity through freshwater removal. The M–O theory considers buoyancy driven by air-sea heat fluxes. However, the atmospheric boundary layer has the additional effects of humidity, which affect both the buoyancy of air and the thermodynamics. Dry, hot air leads to faster evaporation, whereas moister air is more buoyant, thus air-sea fluxes account for these effects of water vapour through the implementation of *virtual temperature*.

$$\overline{w'T_v'}^{0+} \approx \overline{w'T'}^{0+} + 0.61 T_r \overline{w'q'}^{0+} \tag{4.7}$$

The surface buoyancy flux needs to be adapted to include virtual temperature forcing, as does L_a:

$$L_a = \frac{1}{\kappa} \frac{-u_*^3}{\overline{w'b'}^{0+}} = \frac{T_r}{\kappa g} \frac{-u_*^3}{\overline{w'T_v'}^{0+}} = \frac{T_r}{\kappa g} \frac{-u_*^3}{\overline{w'T'}^{0+} + 0.61 T_r \overline{w'q'}^{0+}} = \frac{T_r}{\kappa g} \frac{u_*^2}{T_{*a} + 0.61 T_r q_{*a}}, \tag{4.8}$$

$$b_{*a} = g(T_{*a}/T_r + 0.61 q_{*o}). \tag{4.9}$$

Similarly, in the ocean, the buoyancy flux includes the salinity flux, so

$$L_o = \frac{1}{\kappa} \frac{-u_*^3}{\overline{w'b'}^{0-}} = \frac{1}{\kappa} \frac{-u_*^3}{\beta_T \overline{w'T'}^{0-} - \beta_S \overline{w'S'}^{0-}} = \frac{1}{\kappa} \frac{u_*^2}{\beta_T T_{*o} - \beta_S S_{*o}}, \tag{4.10}$$

$$b_{*o} = g(\beta_T T_{*o} - \beta_S S_{*o}). \tag{4.11}$$

The salinity flux is related to the evaporation minus precipitation at the sea surface. Here a linear equation of state for seawater is assumed, with approximate expansion/contraction coefficients $\beta_T \approx 1.67 \cdot 10^{-4} K^{-1}$, $\beta_S \approx 0.78 \cdot 10^{-4} \text{‰}^{-1}$. Ordinarily, since the M–O theory is intended to be used under turbulent, neutral, convective (evaporating), and stabilising (condensing or precipitating) forcing conditions, we will assume that the freshwater flux (and thus latent heat) can be connected to the turbulent salt flux as in (4.6), rather than stabilising so strongly that the theory doesn't apply (e.g., the perfect fluid thought experiment of Nurser and Griffies, 2019).

Salinity is different dynamically from humidity in many ways. Salinity decreases buoyancy and humidity increases it, but salty water and humid air near the surface both tend to accelerate convection. Both are produced by evaporation, which implies a transfer of latent heat and freshwater from the ocean to the atmosphere (typically as the ocean absorbs excess radiative or sensible heating). For typical oceanic salinities, the evaporation rate is minimally affected by the salinity of the evaporating water. Likewise, the location where precipitation falls on the ocean surface does not depend on the salinity. Thus unlike temperature and humidity, salinity anomalies do not have a major feedback through air-sea processes, thus lateral freshwater sources can bring distant effects (MacKinnon et al., 2016). Salinity fronts often drive adjustments if they are not compensated by temperature gradients, in this form they can persist over long time scales, because they are more stable to air-sea interaction (Rudnick and Ferrari, 1999; Ferrari and Paparella, 2003). However, in the atmosphere, variability in sea surface temperature will drive variations in sensible and latent heat fluxes that may drive interactions within the coupled system, as may humidity gradients drive variations through their effect on latent heat fluxes (4.6).

4.2.2.2 Free convection layers and velocities

An extension of the M–O theory that has long been in use is the concept of free convection velocities. Higher in the atmosphere approaching the capping layer ($z/L_a \ll 1$), and deeper in the ocean layers, approaching the mixed layer base ($z/L_o \ll 1$), destabilising surface conditions lead to convective plumes that extend beyond the surface log-layers into a free convection region. This free convection is normally halted by the mixed layer base or a capping inversion, inducing entrainment. How big is the typical convective velocity?

The free convection velocities (w_*) are useful in describing motion where convection dominates over shear forcing. These velocities are not part of the M–O theory, as they involve a new parameter—the mixed layer depth—that is not prescribed by the surface forcing.

$$w_{*a}^3 = \overline{w_a' b_a'}^{0+} h_a, \qquad w_{*o}^3 = \overline{w_o' b_o'}^{0-} h. \tag{4.12}$$

These buoyancy fluxes should include the humidity and salinity contributions in addition to the buoyancy from anomalous temperatures of air and seawater. Many 1D parameterisations (Section 4.4.2) depend on both the friction and free convection velocities.

One of the smallest submesoscale instabilities, symmetric instability, links to convection within a well-mixed layer, along with more negative z/L transitions into along-isopycnal mixing of tracers and momentum. The depth at which this second effect ends is where the layer over which potential vorticity is well-mixed and opposite in sign to f ends (Thomas et al., 2013; Hamlington et al., 2014; Bachman et al., 2017; Dong et al., 2021). This symmetric instability or PV mixed layer is deeper than the convective (density) mixed layer when symmetric instability is active (Hamlington et al., 2014; Dong et al., 2021).

4.2.2.3 Penetrating radiation

A key difference between the atmosphere and the ocean is the impact of penetrating solar radiation in the ocean. In clear open ocean conditions, there is sunlight appreciably tens to hundreds of metres below the surface. This sunlight warms the ocean *below the surface*, and under certain conditions can trigger convection, because the surface is simultaneously cooled by longwave, sensible, and latent heat fluxes even when the net heating of the ocean is zero. Solar heating (R) occurs at depths (pressures) greater than the cooling (at the surface by $Q_L + Q_S + L$). Were this forcing steady, the situation would resemble the flux Rayleigh–Bénard problem studied by Otero et al. (2002). Under winds, penetrative surface fluxes can also enhance stabilising near-surface ocean boundary layers and result in strong diurnal warm layers (Hughes et al., 2020). The penetrative fluxes on their own tend to be stabilising, because they heat the near-surface more than at depth, but when combined with surface cooling the effect can trigger convection without net surface fluxes. This aspect of the oceanic boundary layer is often neglected in parameterisations and simulations of boundary layer mixing.

4.2.2.4 Budget equations

Consider a free atmosphere velocity $\mathbf{V}_a = (U_a, V_a, W_a)$ and an ocean pycnocline velocity $\mathbf{V}_o = (U_o, V_o, W_o)$. The near-surface layers link these two reservoirs of momentum together, but the turbulence within each boundary layer also allows for deviations in the mean velocity profile from these outer velocities. The horizontally homogeneous momentum equations for the velocities within the boundary layers ($\mathbf{v}_o$, $\mathbf{v}_a$) can be written as

$$\frac{\partial \overline{u}_a}{\partial t} + \frac{\partial \overline{u_a' w_a'}}{\partial z} = f(\overline{v}_a - V_a), \qquad \frac{\partial \overline{v}_a}{\partial t} + \frac{\partial \overline{v_a' w_a'}}{\partial z} = f(U_a - \overline{u}_a); \tag{4.13}$$

$$\frac{\partial \overline{u}_o}{\partial t} + \frac{\partial \overline{u_o' w_o'}}{\partial z} = f(\overline{v}_o - V_o), \qquad \frac{\partial \overline{v}_o}{\partial t} + \frac{\partial \overline{v_o' w_o'}}{\partial z} = f(U_o - \overline{u}_o). \tag{4.14}$$

If we integrate each of these equations from the surface to the extent of their boundary layers, where the turbulence vanishes (or slightly farther so as to have integral bounds fixed in time), multiply each equation by the corresponding background density, then

$$\frac{\partial}{\partial t} \int_0^{h_a} \rho_a \overline{u}_a \mathrm{d}z + \tau_u = f \int_0^{h_a} \rho_a (\overline{v}_a - V_a) \mathrm{d}z, \quad \frac{\partial}{\partial t} \int_0^{h_a} \rho_a \overline{v}_a \mathrm{d}z + \tau_v = f \int_0^{h_a} \rho_a (U_a - \overline{u}_a) \mathrm{d}z; \tag{4.15}$$

$$\frac{\partial}{\partial t} \int_{-h}^0 \rho_o \overline{u}_o \mathrm{d}z - \tau_u = f \int_{-h}^0 \rho_o (\overline{v}_o - V_o) \mathrm{d}z, \quad \frac{\partial}{\partial t} \int_{-h}^0 \rho_o \overline{u}_o \mathrm{d}z - \tau_v = f \int_{-h}^0 \rho_o (U_o - \overline{u}_o) \mathrm{d}z. \tag{4.16}$$

Note that τ transfers momentum from the atmosphere to the ocean. Relatedly, in steady state the (turbulent) Ekman transport is given by the right-hand integral in each equation; it is an anomaly from the free atmosphere and free ocean velocity, and the Ekman mass transport in the atmosphere is equal and opposite to the Ekman mass transport in the ocean. Considering the effect of the time dependence, it is clear that an inertial oscillation can be superimposed on the atmosphere or ocean without necessarily affecting the air-sea fluxes, unless τ at the surface changes to oscillate as well.

Note that although we have neglected horizontal variations in properties, often the free atmosphere velocity $\mathbf{V}_a$ and the ocean pycnocline velocity $\mathbf{V}_o$ are assumed to be geostrophic, which then implies that the pressure does vary in the horizontal direction. Taking this thinking farther, if these velocities are also hydrostatic, the vertical derivative of (4.13)–(4.14) results in a steady-state balance called the turbulent thermal wind balance (TTW; McWilliams (2016)). This balance is fundamental to submesoscale-boundary layer turbulence interactions at baroclinic fronts, and relates lateral gradients in density to baroclinic shear in the boundary layer—affected by turbulent vertical momentum fluxes as well. It is possible that the free atmosphere and ocean pycnocline velocities are in geostrophic balance with barotropic pressure anomalies, which would leave shear in the boundary layers as turbulent Ekman anomalies as in (4.15)–(4.16).

If the location in consideration is not in the centre of a submesoscale front, then lateral density gradients and baroclinicity are expected to be small. Monin and Obukhov (1954) go on to argue that the Coriolis parameter and time dependence may also be neglected near the surface. In this case, dimensional analysis proposes that the gradients in each profile property depend only on the fluxes, the distance from the boundary, and the M–O depth, or

$$\frac{\kappa z}{u_{*a}}\frac{\partial \overline{v}_a}{\partial z} = \phi_m\left(\frac{z}{L_a}\right), \qquad \frac{\kappa z}{T_{*a}}\frac{\partial \overline{T}_a}{\partial z} = \phi_h\left(\frac{z}{L_a}\right), \qquad \frac{\kappa z}{q_{*a}}\frac{\partial \overline{q}_a}{\partial z} = \phi_c\left(\frac{z}{L_a}\right); \tag{4.17}$$

$$\frac{\kappa z}{u_{*o}}\frac{\partial \overline{v}_o}{\partial z} = \phi_m\left(\frac{z}{L_o}\right), \qquad \frac{\kappa z}{T_{*o}}\frac{\partial \overline{T}_o}{\partial z} = \phi_h\left(\frac{z}{L_o}\right), \qquad \frac{\kappa z}{S_{*o}}\frac{\partial \overline{S}_o}{\partial z} = \phi_c\left(\frac{z}{L_o}\right). \tag{4.18}$$

The log layer behaviour is found by recognising all these similarity functions should go to one as z approaches zero. These similarity functions are universal, so long as the assumptions of M–O theory hold, so the same functions should apply in the atmosphere and ocean. The functions do differ depending on the sign of z/L, so there is different behaviour under convective ($z/L < 0$), neutral ($z/L = 0$), and stabilising ($z/L > 0$) forcing. Högström (1996) and Wyngaard (2010) provide many examples of empirical fits based on observations.

The fluxes of buoyancy, salinity, and temperature consistent with the similarity functions above can be found from the conservation equations, as can equivalent eddy diffusivity and viscosity functions. This approach provides a partial basis for many of the 1D parameterisations (Section 4.4.2).

Another primary basis for parameterisations and observation are the equations for conservation of energy, thermal, potential, and mechanical. In Boussinesq fluids, the thermal energy equation is decoupled from the others (and amounts to an equivalent of the conservation of temperature). The kinetic energy, temperature variance, and buoyancy transport equations are (written here for the ocean, but equivalent in the atmosphere as well), again assuming no lateral variations of any statistics:

$$\underbrace{\frac{\partial}{\partial t}\frac{\overline{\mathbf{u}'_o \cdot \mathbf{u}'_o}}{2}}_{\text{TKE tend.}} + \underbrace{\overline{\mathbf{u}'_o w'_o}\frac{\rho_o \partial \overline{\mathbf{u}}_o}{\partial z}}_{\text{shear prod.}} + \underbrace{\frac{\partial}{\partial z}\frac{\overline{\mathbf{u}'_o \cdot \mathbf{u}'_o w'_o}}{2}}_{\text{TKE transport}} = \underbrace{-\frac{1}{\rho_o}\frac{\partial}{\partial z}\overline{p'w'}}_{\text{pressure work}} + \underbrace{\overline{w'b'}}_{\text{buoy. prod.}} - \underbrace{\epsilon}_{\text{diss.}}, \tag{4.19}$$

$$\underbrace{\frac{\partial}{\partial t}\frac{\overline{T'^2_o}}{2}}_{\text{Var. tend.}} + \underbrace{\overline{w'_o T'_o}\frac{\partial \overline{T}_o}{\partial z}}_{\text{prod.}} = \underbrace{\chi}_{\text{diss.}}, \tag{4.20}$$

$$\underbrace{\frac{\partial}{\partial t}\frac{\overline{w'_o b'_o}}{2}}_{\text{Flux tend.}} + \underbrace{\overline{w'^2_o}\frac{\partial \overline{b}_o}{\partial z}}_{\text{prod.}} + \underbrace{\overline{b'_o w'_o}\frac{\partial \overline{w}_o}{\partial z}}_{\text{prod.}} = -\overline{b'^2_o} + \underbrace{\upsilon}_{\text{diss.}}. \tag{4.21}$$

These are examples of second-moment equations, of the type underlying a particular class of parameterisations (Section 4.4.2.3). For examples of how these equations may be scaled by extending the M–O theory, see Grant and Belcher (2009) and Belcher et al. (2012).

Potential energy, e.g., from unstable stratification, including humidity (leading to convective available potential energy, or CAPE) and salinity effects can be converted into kinetic energy through the buoyancy production term. Alternatively,

stratification can be destroyed (i.e., mixed) at the cost of buoyancy production. Note that penetrating solar radiation can lead to positive buoyancy production, thus making the ocean act as a heat engine or Carnot cycle with solar radiation and surface cooling as the thermal reservoirs. Precipitation also removes moisture from the air and adds it to the ocean, although the latent energy released during condensation before precipitation tends to affect the cloud layer rather than the surface. The sensible heating or cooling of the ocean surface due to precipitation at a different temperature is typically neglected. Latent heat during snow falling on the ocean can be significant (e.g., Ledley, 1991).

The temperature variance equation is also a useful budget to consider when making measurements of dissipation (Section 4.3). The buoyancy flux tendency equation is a bit unfamiliar perhaps, but it is formed in a similar manner to the other two equations and it serves to illustrate that fluxes also have a budget, although they are not materially conserved in perfect fluids.

4.2.2.5 Time-varying forcing

While the M–O theory and many modelling studies use constant-in-time forcing and statistically steady budgets, in most ocean regions diurnal, synoptic, and seasonal variability is critical to understanding the upper ocean layers. Only for brief moments in the morning and afternoon are the conditions within the whole atmospheric boundary layer approximately neutral, instead convective or stabilising boundary conditions are typical. Similarly, the ocean varies back and forth through stabilising and convective conditions, but even when the surface flux is zero the near-surface ocean can be driven toward convection by the penetrating solar radiation. Interestingly, the ocean is destabilised at night and stabilised during the day, whereas the atmosphere is opposite. Note that just using the daily-averaged solar radiation is not a good approximation, as mixing and restratification are distinct processes with significant irreversibility. The atmospheric boundary layer is also significantly different under convection (including rainfall) and subsidence due to the precipitation on updrafts and the related thermodynamic and buoyancy implications.

Additionally, over the past decade significant resources have been exerted into understanding the forcing and implications of near-inertial oscillations. These phenomena are readily excited by high-frequency winds and can drive significant shear near the mixed layer base and entrainment (Jochum et al., 2013; Alford et al., 2016). Cyclones drive a rapid mixed layer deepening to one side of the eye of the storm due to wind circulations that resonate with inertial excitations (Sanford et al., 2007).

While the M–O scaling parameters are still useful quantifications of the magnitude of forcing, when time-dependence is involved other aspects of the problem enter and a similarity solution is not readily found. Both the initial conditions and present conditions affect the boundary layer in this case (Pearson et al., 2015).

4.2.2.6 Lateral variation

As in the case of time-varying forcing, when fluxes vary laterally the M–O theory fails and other parameters enter. The case above of baroclinicity arising from a submesoscale front is an excellent example. The response of the atmospheric boundary to this case is studied by Sullivan et al. (2020), but the oceanic front case is also interesting (e.g., Hamlington et al., 2014; Taylor, 2018; Bodner et al., 2020), especially the turbulent thermal wind balance and its consequences (McWilliams, 2016). Note that while the turbulent Ekman case described above is almost trivial, considering Ekman pumping requires lateral variations, vertical vorticity of free atmosphere winds or pycnocline velocity, and surface divergence within the layer. For this reason, Ekman pumping goes beyond the M–O theory (although it is illustrated in Fig. 4.2).

The turbulent thermal wind (TTW) is another approach as to how lateral variations and turbulent mixing can be combined. The basic principle is that a three-way balance that adds turbulent mixing into the thermal wind relation captures important aspects of turbulence acting on fronts. This theory has been applied to analysis of simulations (McWilliams et al., 2015; Sullivan and McWilliams, 2019) and in analytic work (Crowe and Taylor, 2018; Bodner et al., 2020) recently.

4.2.2.7 Waves

Perhaps most of the effort in pushing oceanic boundary layer theory outside of the reach of M–O theory in the past decade has involved surface waves. This section will discuss some ways that waves do not fit into the M–O theory.

A variety of papers have reworked the M–O approach to include aspects of waves. Large et al. (2019) is a recent example, where a separable similarity function assumption is made, with the standard similarity function multiplied by a function depending on the turbulent Langmuir number,

$$La_t^2 = \frac{u_{*o}}{u_s^{0^-}}, \tag{4.22}$$

where $u_s^{0^-}$ is the surface Stokes drift speed of the surface waves. However, this is only one of many possible wave parameters to include from the wave field: in CESM2, the wave model has nearly 10 times as many degrees of freedom as the whole ocean model profile to depth on the same horizontal grid (Li et al., 2017).

In the past, because most wave energy is carried in wind waves that eventually equilibrate to τ, it was assumed that there was no need to include wave properties outside of τ which is already part of the M–O theory (e.g., McWilliams and Restrepo, 1999). However, when operational wave models were used to test this hypothesis, it was found that waves are rarely in equilibrium in direction (Hanley et al., 2010), or magnitude, frequency, and penetration depth (Webb and Fox-Kemper, 2011), or in uniformity of direction (Webb and Fox-Kemper, 2015). Instead, surface waves tend to spread out in direction and may propagate long distances from their origin as swell. What does this amount to in wave impacts on boundary layers? It is important to note that careful observations do detect systematic differences between M–O theory predictions and turbulence statistics that are consistent with some theories of wave-enhanced turbulence (D'Asaro, 2014; D'Asaro et al., 2014; Sutherland et al., 2013, 2014; Zheng et al., 2021). The Charnock (1955) scaling for wind stress given wind speed does include waves, but only in a modest dimensional analysis manner. Non-equilibrium waves (which would depend on initial wave state) and remotely-generated waves (which depends on conditions elsewhere, e.g., crossing swell) are not part of Charnock's scaling. So, a key question is to what extent disequilibrium waves are important.

A first series of efforts were carried out to examine the effects of breaking waves, albedo from whitecaps, spray, etc. (see Cavaleri et al., 2012, for a review). These effects are often small on average, but some are predictable and have been parameterised in their impact on air-sea fluxes primarily (Section 4.2.2.10) and secondarily on surface transport properties (see Lenain and Pizzo, 2020, for a recent example). These are not disequilibrium events; indeed they are part of what allows for fully developed wave states to occur (Sullivan et al., 2004). Zheng et al. (2021) show a variety of ways that observations, especially profiles of temperature, are inconsistent with M–O theory but are consistent with wave breaking and Langmuir turbulence theory.

The depth to which wave effects penetrate is a key aspect of the wave problem, and is a disequilibrium situation as it takes some time for the mean wave period to arrive at a fully developed value (Webb and Fox-Kemper, 2011). Like the penetrating solar problem, it violates the assumption of the M–O theory that all of the effects take place near the surface. One approach is to consider the vertical decay scale of the orbital velocity, which is proportional to the wavelength of the waves (Qiao et al., 2004, 2010). Other approaches use the Stokes drift decay scale, or more precisely, an average of Stokes drift effects over a fraction of the boundary layer (Harcourt and D'Asaro, 2008; Van Roekel et al., 2012; Li et al., 2016). Because the Stokes drift decay scale tracks closely over seasons and forcing with the orbital velocity decay scale, both approaches yield similar sensitivity to wave states.

Entrainment is an important result of deeply penetrating Langmuir turbulence or non-breaking wave turbulence. Langmuir jets penetrate much more deeply than the shallow Stokes drift that enhances them (Polton and Belcher, 2007). Langmuir entrainment has important consequences for passive tracers (Smith et al., 2016) and mixed layer deepening (Li et al., 2017). Entrainment is elevated even when Langmuir cells (as recognised by their form, anisotropy, and turbulence statistics) do not reach the mixed layer base (Li and Fox-Kemper, 2020). Thus observations of Langmuir cells remaining trapped in the upper mixed layer do not imply that wave-enhanced mixing does not accelerate entrainment (as suggested by, e.g., Weller and Price, 1988; Thorpe et al., 2003); it does so by enhancing the shear near the mixed layer base via pressure work.

Non-breaking surface waves had not been considered to be able generate turbulence, because the governing equation of non-breaking surface waves is simplified as irrotational mathematically (Phillips, 1961). However, the groundbreaking work of Teixeira and Belcher (2002) showed that if there is vorticity already in turbulence in the ocean, then passing irrotational waves can intensify it. This conception is consistent with both the theory of Langmuir turbulence, effectively defined to be the class of turbulence that arises in simulations of the Craik–Leibovich or wave-averaged equations that include a Stokes vortex or Stokes shear force (McWilliams et al., 1997; Holm, 1996; Suzuki et al., 2016; Holm and Hu, 2021), often by comparison to large eddy simulations of these equations (Section 4.4.1). An important aspect to understand about the wave-averaged equations is that the only wave information that appears in them is the Stokes drift profile, hence the approach of Large et al. (2019) and the focus on Stokes drift in Webb and Fox-Kemper (2011, 2015). The non-breaking surface waves theory seeks to similarly explain the enhanced turbulence due to the presence of surface waves. The non-breaking surface-wave-induced vertical mixing scheme (Bv), however, does not phase-average the effect and instead relies on high-frequency observations of laboratory and field sites to study the enhancement effect (e.g., Qiao et al., 2016). Qiao et al. (2016) provided solid experimental evidence of wave-turbulence interactions in the ocean directly for the first time, by employing the newly developed Holo–Hilbert spectral analysis (Huang et al., 2016). Pragmatically, the distinction between the two theories lies in whether mixing varies more directly in response to the orbital velocity characteristics (non-breaking
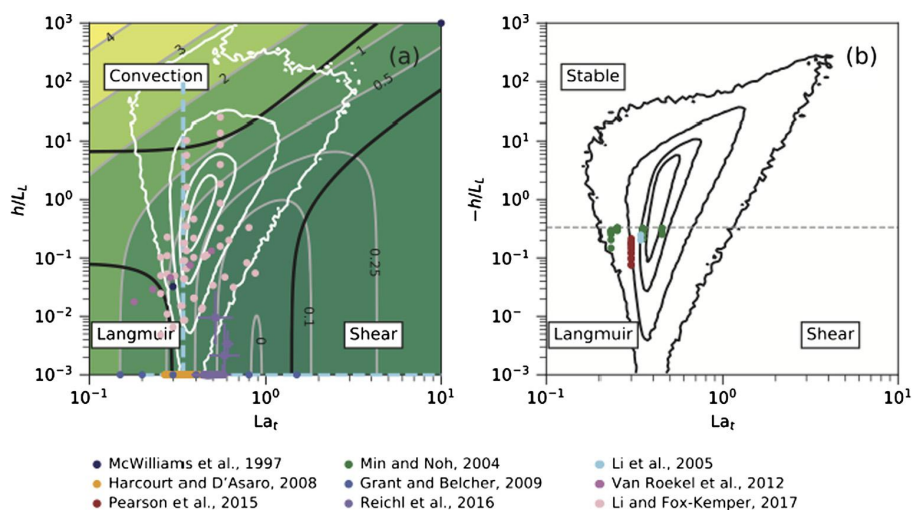
FIGURE 4.3 Regime diagram of Langmuir forcing of the world oceans based on JRA55-do (Tsujino et al., 2020) forcing reproduced with permission from (Li et al., 2019) following Belcher et al. (2012). The location where large eddy simulations of the wave-averaged equations have been performed are indicated by dots (McWilliams et al., 1997; Harcourt and D'Asaro, 2008; Pearson et al., 2015; Min and Noh, 2004; Grant and Belcher, 2009; Reichl et al., 2016; Li et al., 2005; Van Roekel et al., 2012; Li and Fox-Kemper, 2017). (a) Regions and seasons where convective forcing is present, indicating in solid lines, where 90% of the dissipated energy comes from convective, Langmuir (i.e., Stokes shear production), or shear production. (b) Regions and seasons where convective forcing is stabilising (e.g., surface warming). Above the dotted line, turbulence is expected to be only transient, whereas below the Langmuir or shear forcing exceeds the stabilising buoyancy forcing.

theory) or the Stokes drift statistics (Langmuir turbulence), although it can be challenging to distinguish them as they co-vary.

Another wave parameter that is important for the effects of Langmuir turbulence is the degree of misalignment of waves and winds. Hanley et al. (2010) showed that this was a common occurrence, and Van Roekel et al. (2012) showed that a simple approach of projecting waves and winds into the direction of the forming Langmuir cells collapses many misalignment cases onto the same profile. Van Roekel et al. (2012) go on to suggest that a redefined Langmuir number can capture both the misalignment and the depth effects (following Harcourt and D'Asaro, 2008) in one parameter, simplifying the dimensional analysis. Other studies of wave-wind misalignment have found that this simple approach is fairly robust, but could be improved (Sullivan et al., 2012; Wang et al., 2019a).

In Belcher et al. (2012), an important outcome was the establishment of a regime diagram based on the sources of energy, similar to scaling (4.19), but including Stokes forces. This same diagram was expanded upon and more carefully evaluated in Li et al. (2019) and is reproduced in Fig. 4.3. The vertical axis shows a dimensionless parameter that is similar to the boundary layer depth over the M–O length, but including wave effects. When this parameter is negative (right panel), the surface forcing is warming and stabilising. When it is positive, it is tending to convect—more strongly, the larger its magnitude. Along the horizontal axis is the turbulent Langmuir number, which indicates the relative amount of winds (to the right) versus waves (to the left). The regime diagram thus indicates the regions where convection, Langmuir forcing (i.e., wave energy), and wind forcing are most important. The white triangular contours map where realistic forcing of the world ocean places the highest likelihood. Coloured dots indicate where large eddy simulations have been carried out.

Li et al. (2019) also show that even among Langmuir schemes that purport to include the same effects and converge to the same LES there are considerable differences in the outcomes of applying the different schemes based on physical and numerical formulation. The same is likely true of the non-breaking wave approaches. Johnson et al. (2021) explore a dynamical systems approach to quantifying the divergent behaviours of different schemes under a variety of forcings.

4.2.2.8 Waves and momentum

Along with the wind-wave misalignment problem comes the general nature of the Stokes vortex or Stokes shear force (Suzuki and Fox-Kemper, 2016). This effect results in a downward force, acting like a density anomaly in the hydrostatic or nonhydrostatic equations, that is directional: only when the Lagrangian current (the combination of Eulerian mean current and Stokes drift) is oriented along the Stokes drift direction does this force maximise. When the current and waves are opposed, it is an upward force, and when they are perpendicular, it is zero.

This conceptualisation simplifies the mechanism for Langmuir turbulence. Langmuir cells converge when surface currents randomly flow in the Stokes drift direction. This causes convergences which strengthens the jets, forms turbulence and can accelerate frontogenesis (Suzuki et al., 2016) and filamentogenesis (Sullivan and McWilliams, 2019).

The air-sea transfer coefficient c_d is also likely directional. In the presence of crossing swell, there should be favoured directions for efficient momentum transfer (winds into swell) and others that are less so (winds behind swell or crossing across swell). The anisotropy of the drag coefficient (and likely also the heat and moisture coefficients, due to the changing near-surface airflow) implies that the relative velocity to stress relationship in (4.4) is probably an oversimplification, and the drag coefficient should instead be a second-rank tensor that depends on swell propagation direction.

4.2.2.9   Sea ice

As the sea ice interface sets the surface boundary conditions, stress at the ice-ocean interface depends on undersurface roughness, thereby altering u_*, whereas melting/freezing ice induce a negative/positive buoyancy flux, respectively. In the neutral limit, McPhee and Martinson (1994) show the importance of kinematic boundary stress and Ekman dynamics on turbulent mixing lengths, often incorporating rotation not included in the M–O theory. In the presence of stable (McPhee, 1994) or unstable (McPhee and Stanton, 1996) freshwater fluxes, similarity theory can be modified to account for distance from the ice, freshwater buoyancy flux, surface stress, and boundary layer stratification.

Sea ice leads to lateral intermittency in the ocean, as waves, fluxes, and albedo are strongly inhibited by the presence of sea ice. Under Arctic climate change, it is expected that a newly revealed ocean boundary layer will be in regular contact with the atmosphere during the Arctic summertime later this century. The opening up of the Arctic has consequences for planetary albedo (e.g., radiation arriving at the ocean), air-sea heat fluxes, and ocean heat uptake and surface waves in the Arctic. Recent studies have covered some aspects of these dynamics and their impact on expected changes (e.g., Horvat et al., 2016; Mensa and Timmermans, 2017; Manucharyan and Thompson, 2017; Roach et al., 2018).

4.2.2.10   Bubbles, spray, whitecaps, & foam

Like sea ice, bubbles, spray, and foam are multiphase phenomena that exist within the near-boundary layers. Bubbles and spray strongly affect the surface area, and thus can be important in air-sea fluxes, as well as in buoyancy effect (e.g., Liang et al., 2013, 2017). Foam, and other persistent surface anomalies, such as biological surfactants, can strongly affect surface roughness and wave dynamics (Cavaleri et al., 2012). Intriguingly, even the intermittent, stochastic forcing of rain droplets can interfere with the formation of coherent small-scale waves, thus affecting roughness and stress (Cavaleri et al., 2015; Zhao et al., 2017). At high wind speeds, bubbles and spray form some of the most challenging aspects of simulating and observing conditions (e.g., Soloviev et al., 2014). The fundamental scaling aspects of these "mushy layer" as opposed to surface problems remain highly speculative, as direct modelling of multiscale, multiphase fluids is not sufficiently advanced. Zhao et al. (2017) and Bao et al. (2020) demonstrate that parameterisations indicate a key role of sea spray in the simulation and prediction of typhoons and the climate system respectively.

4.2.2.11   Shallow water

In very shallow water, the ocean surface and bottom boundary layers merge, so that the whole depth is diabatic and turbulent. Studies on Langmuir super-cells (Gargett et al., 2004) follow the consequences into bottom boundary impacts of these surface-forced phenomena. Many shallow estuaries have essentially no vertical stratification during wintertime, which makes the lateral salinity and temperature gradients key to understanding the flow (e.g., Codiga and Ullman, 2010; O'Donnell et al., 2014; Jing et al., 2016).

4.2.3   Mixed layers: boundary layer memory

The mixed layer of the ocean in schematic form is straightforward (Fig. 4.2): how deep has the turbulent mixing homogenised the vertical temperature and salinity fields? But in practice the temporal and spatial variability and poor subsurface sampling lead to many issues in determining the mixed layer depth conclusively. The surface forcing in a particular place and time has little to do with the previous forcing and potentially also restratification processes that have brought the mixed layer to its present properties. There are thus a variety of definitions of mixed layer, which are very briefly summarised here. Some aspects of the dynamical significance of the different methods are also given.

The mixed layer is typical found based on one of two approaches: (1) a threshold for when deep properties have gone "far enough" away from their surface value to be different, and (2) when tracer values exceed a relative level of variability that is determined in the same region or cast. A critical breakthrough for either method was found by de Boyer Montégut
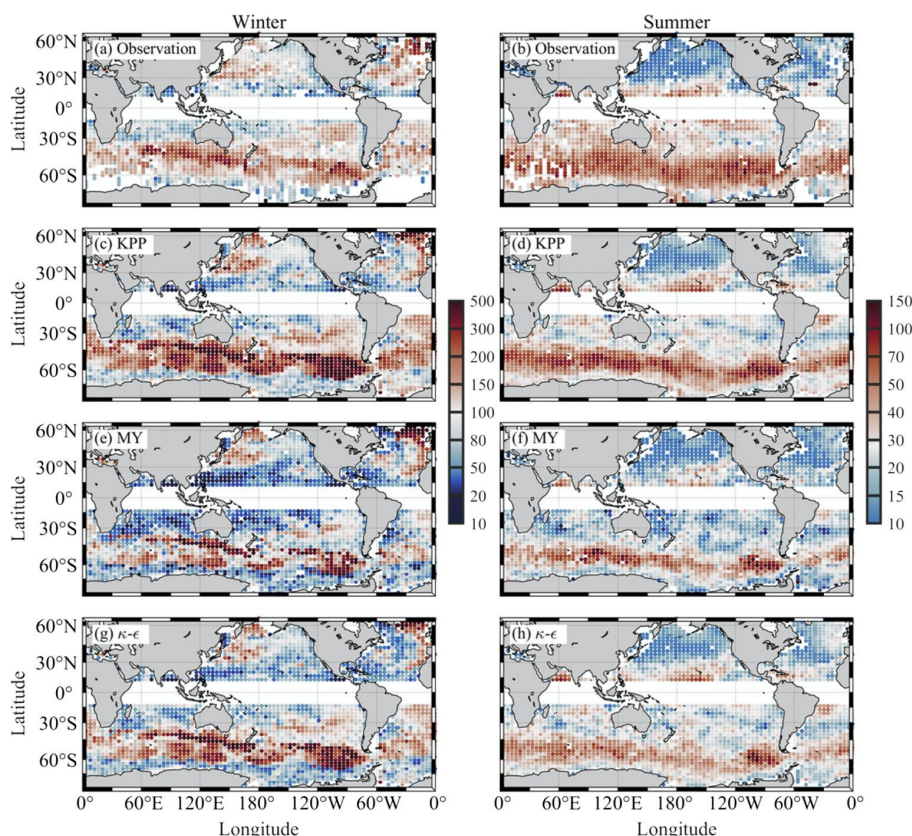
FIGURE 4.4 Mixed-layer depth m as determined using the (Huang et al., 2018) method from 2010–2019 Argo profiles in February and September (by summer and winter in both hemispheres) and 1D simulations of the generalised ocean turbulence model in the same seasons (Umlauf and Burchard, 2005) initialised from profiles and using surface forcing from a global MITgcm simulation (Su et al., 2018). Reproduced with permission from Dong et al. (2020).

et al. (2004). They noted that calculation of the mixed layer depth by most methods and lateral averaging of the properties (salinity, temperature, density) from observational profiles do not commute. That is, if you calculate the mixed layer depth on the mean properties (e.g., Monterey and Levitus, 1997) you do not get the same answer as when you calculate the mixed layer depth on each observational profile, and then laterally average. Similarly, when a simulation is initialised from observations, it should be initialised from a single profile, not an average (e.g., D'Asaro et al., 2014). The latter is clearly the more important approach for the dynamics discussed in this chapter. Other authors have continued to improve algorithms using the profile approach (Holte et al., 2017; Huang et al., 2018); quite a few others are reviewed in Dong et al. (2021) and Li et al. (2019).

The boundary layer can be observed in terms of turbulence dissipation with specialised observations, but the mixed layer relies on definitions of what scale of change indicates leaving the boundary. As noted by de Boyer Montégut et al. (2004) and Holte et al. (2017), there is no simple threshold on temperature or density change from the surface value that is reliable worldwide. Even what variable should be used is subject to interpretation: temperature, density, potential vorticity? The relative variance methods have the advantage that presumably the variability that is in the same profile cast gives some sense of the range of surface forcing variability typical of the location (indeed, that is the purpose of L). However, these algorithms tend to have a pattern recognition rather than a dynamical determination of relevant thresholds and limits, thus they too disagree among themselves.

Fortunately, (or unfortunately depending on your perspective) parameterisations of mixed layer processes tend to disagree more than definitions of mixed layers (Li et al., 2019), so for model-observation comparisons one is free to choose among reasonable definitions. Fig. 4.4 shows observed mixed layer depths versus 1D mixing models initialised from a high-resolution model, and then allowed to simulate ocean near-surface layer turbulent mixing (Dong et al., 2021).

4.2.3.1   Entrainment

This chapter has emphasised the air-sea exchange of properties, but perhaps even more societally significant is the exchange of properties across the mixed layer base to the deep ocean. Below the climatic implications of this statement will be described, but here it is important to lay out the dynamics involved in exchanges of properties between the mixed layer and the interior.

As described above, entrainment is a process whereby turbulence escapes the mixed layer to penetrate into the stratified fluids below. By homogenising the properties, the mixed layer deepens and becomes more dense because of this entrained fluid.

Entrainment is a highly complex process, however, and difficult to model and observe due to its intermittent character. Though wind-driven entrainment is a principle concept for OSBL evolution (e.g., Pollard et al., 1973; Price, 1979) and a foundation for upper-ocean mixing model validation (Mellor and Yamada, 1982; Large and Crawford, 1995), intermodel comparison reveals turbulence parameterisations fail to agree on how to deepen the mixed layer in practice (e.g., Li et al., 2019; Johnson et al., 2021). However, recent models (Li and Fox-Kemper, 2017; Van Roekel et al., 2018; Li and Fox-Kemper, 2020; Souza et al., 2020) and some observational analyses (D'Asaro, 2003) have managed to capture entrainment in a statistically and dynamically meaningful way. Given the important role of entrainment in the earth system, it has not received enough study.

4.2.3.2   Restratification

A restratifying mixed layer influences the climate reservoirs on both sides of its boundaries. With the atmospheric boundary layer through its transfer of heat and momentum–i.e., (4.15)–(4.16)–and with the ocean interior as the deeper mixed layer restratifies and joins the pycnocline. The implications of this latter process are featured in the Stommel (1979) demon idea: only the deepest wintertime mixed layer properties are permitted to stratify and join the stratified interior. In contrast to entrainment, which incorporates tracers and momentum from the underlying water, restratification decreases the volume of the mixed layer, but not its intrinsic properties.

Restratification in the ocean can be caused by the following: penetrating solar radiation (which decays exponentially, and thus heats the surface more quickly than deeper waters); surface heating by longwave or warm, moist air; winds that blow light water over dense (i.e., upfront winds); precipitation and condensation of fresh water; or dynamical restratification that extracts potential energy by sorting lighter waters to move above denser. Restratification is a determinative aspect of whether the mixed layer and mixing layer differ, as rapid restratification will tend to push the mixed layer toward the mixing layer, whereas leisurely restratification will allow patterns of mixing to become fossilised in mixed layers far deeper than presently active mixing.

Mixed layer instabilities, and baroclinic instabilities in general, extract energy from the potential energy inherent in stratification anomalies (Boccaletti et al., 2007; Fox-Kemper et al., 2008). The stratification anomalies do not have to be in contact with the surface for the mixed layer instabilities to arise. Submesoscale eddies formed from such instabilities are an important mechanism for restratification at the base of the mixed layer, where often solar restratification and Ekman buoyancy fluxes do not penetrate (Haney et al., 2012).

In addition to baroclinic instabilities, frontal restratification by other mechanisms can influence the upper ocean buoyancy budget. Processes involved include when horizontal buoyancy gradients are differentially advected by near inertial shear (Hosegood et al., 2006), time dependent Ekman dynamics (Dauhajre and McWilliams, 2018; Johnson et al., 2020), or gravity bores (Dale et al., 2008; Pham and Sarkar, 2018).

4.2.4   A home for submesoscales

The small scale of the submesoscale can be considered to be a consequence of the deformation radius ($L_d = Nh/f$) of the mixed layer (Thomas et al., 2008; Dong et al., 2020). The deformation radius of the mixed layer is much smaller than the deformation radius of the whole water column, as the mixed layer is shallower and less stratified.

Submesoscales are also often energised by the extraction of potential energy. This extraction implies a restratification, just as mixing implies a source of potential energy. Whereas submesoscale phenomena may not be the fastest agent of restratification, they are important in that they can act below the surface, remote from where winds and solar restratification are strong. Fig. 4.5 shows the buoyancy frequency, (i.e., $N = \sqrt{\partial b / \partial z}$) within the mixed layer for the same models. As argued in (Dong et al., 2021), the disagreement in stratification within the mixed layer has a larger impact on many aspects of submesoscale dynamics than disagreement in mixed layer depth.
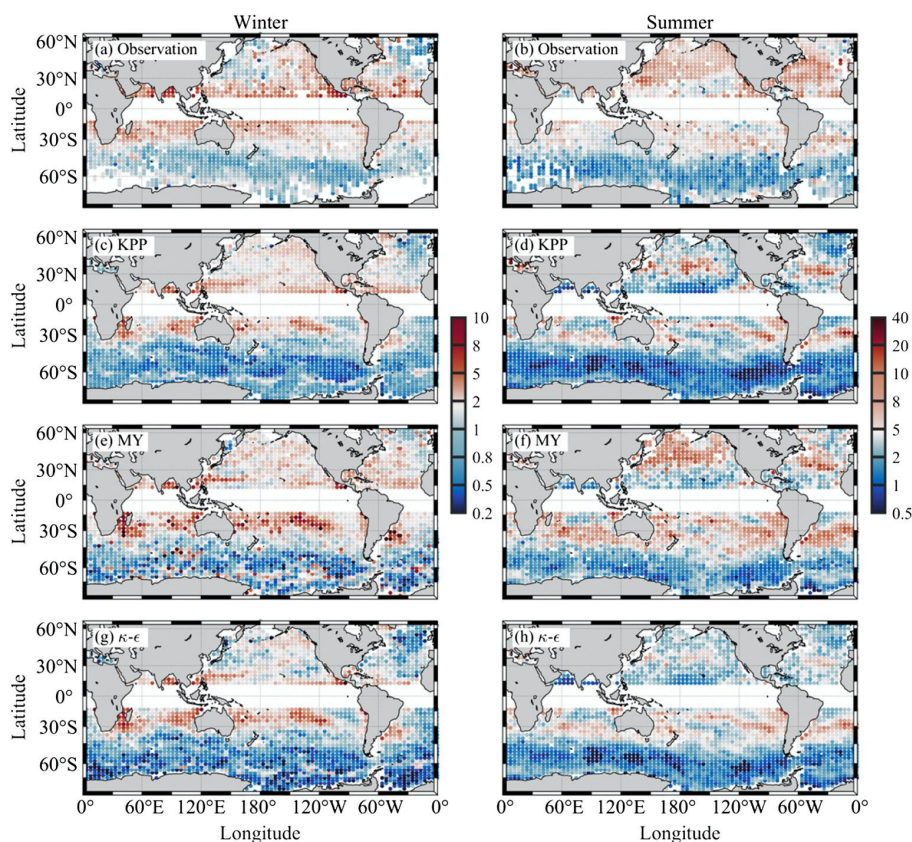
FIGURE 4.5 Buoyancy frequency in the mixed layer ($\times 10^{-3}$ s^{-1}) as determined from 2010–2019 Argo profiles in February and September (by summer and winter in both hemispheres) and 1D simulations of the generalised ocean turbulence model in the same seasons Umlauf et al. (2016), initialised from profiles and forced with surface forcing from a global MITgcm simulation (Su et al., 2018). Reproduced with permission from Dong et al. (2020).

4.3 Observing the surface layers and their processes

4.3.1 Observing mixing

Mixing in the ocean surface boundary layer (OSBL) can be inferred over a range of complexities depending on the topics of interest and/or measurement capabilities available. A description of technological advancements in ocean mixing observations are detailed in Chapter 14, but a quick review of observations specific to the OSBL layer are included here. Measurements of turbulent quantities within the OSBL are complicated, particularly by the span of turbulent motions from centimetres to the entire length of the mixed layer, and therefore require different approaches than methods used to measure turbulence in the ocean interior. As such, turbulence estimates can be drawn from a range of parameters, including vertical profiles of mean temperature, salinity, and velocity and their vertical gradients, turbulent fluxes, the reduction of temperature variance by turbulence χ, and dissipation of turbulent kinetic energy, ϵ. Additionally, turbulent quantities in the boundary layer are orders of magnitude larger than in the interior and coexist with a complicated wave field, both of which contribute to challenges in making meaningful measurements and require different platforms than the relatively quiescent interior.

4.3.1.1 Defining mixing from mean profiles

Routine and accessible metrics for mixing in the upper ocean can be obtained from profiles of mean tracers T, S, and velocities u, v. Most common is to assume quantities are homogeneous over a mixed layer depth h, using some of the methods in Section 4.2.3. In the atmosphere, profiles of mean shear are often used to constrain vertical fluxes, but this approach has not been successfully carried out in the ocean (except in large eddy simulations, Large et al., 2019). Yet, more active definitions isolate the processes of mixing. For example, shear driven turbulence can be identified through the ratio

between shear and stratification as the Richardson number $Ri = N^2/|\partial_z u|^2$, where turbulence is suppressed at a critical value $Ri > 1/4$. Or in a mixed layer undergoing deep convection, the upper ocean may be unstably stratified ($N^2 < 0$), and ocean mixing can be inferred through the Thorpe scale (Thorpe, 2007).

All of these methods have been widely adopted to pertain to observations of the boundary layer with the common measurements collected by CTD instruments (conductivity, temperature, and depth) and ADCPs or ADVs (Acoustic doppler current profilers or Acoustic doppler velocimeters). Vertical profiles may be obtained through shipboard surveys with profiling instruments, Lagrangian floats (Harcourt et al., 2002), profiling drifters (e.g., Argo: Roemmich et al., 2019), gliders (e.g., Sea Glider, Slocum Javaid et al., 2014), or autonomous profilers (e.g., WireWalker: Pinkel et al., 2011). Whereas CTDs are standard on most observational platforms, obtaining accurate velocities from ADCPs are challenging in the near-surface layers, yet are becoming smaller and more common on autonomous platforms. A large contribution to boundary-layer mixing has come from very high resolution measurements of mean properties (such as thermistor chains and the Surf Otter), and platforms that can obtain near-surface meteorological data and subsurface measurements (Gentemann et al., 2020; Pinkel et al., 2011; Edson et al., 2007).

4.3.1.2 Estimating turbulent fluxes

Obtaining a more dynamical view of upper ocean mixing requires estimates of turbulent quantities v', w', C' and their turbulent covariances and fluxes $\langle v'^2 \rangle$, $\langle w'^2 \rangle$ and $\langle C'w' \rangle$. Yet turbulent velocity fluctuations are often obscured by the ~ 100 times larger surface wave induced velocities. To address this, turbulent vertical velocity can be estimated from a neutrally buoyant Lagrangian float (D'Asaro, 2003). In the OSBL, the float traverses the mixed layer along with the largest eddies, through which vertical velocity statistics can be calculated from the rate of pressure change. Based on this approach, D'Asaro et al. (2014) were able to show that over a wide range of wind and wave conditions, the vertical velocity statistics are *inconsistent* with the standard M–O scaling for oceanic boundary layers, but are consistent with the scaling of statistics expected based on one of the wave-driven turbulence theories (Harcourt and D'Asaro, 2008). Similarly, based on observations from two fixed offshore platforms, Chen et al. (2018, 2019) investigated the atmospheric boundary layer, particularly how surface waves modulate air-sea momentum flux, and explained the deviation of the wind stress from the wind direction under low to moderate wind conditions, indicating upward momentum transfer from the ocean to the atmosphere through surface waves.

Momentum flux (or turbulent Reynolds stress) in the OSBL is generally assumed to be equal to, at least no more than, the wind stress over the sea surface in ocean and climate models based on traditional boundary-layer theory. However, simultaneous in-situ observations conducted by Huang and Qiao (2021) show, for the first time, that the turbulent Reynolds stress in the OSBL is modulated greatly by surface waves and can be larger than the wind stress in certain circumstances. This observational result may have a potential impact on the development of ocean and climate models.

4.3.1.3 Dissipation and loss of shear and temperature variance

Values of kinetic energy dissipation ϵ and temperature variance dissipation χ are inferred through measurements of high-frequency fluctuations in velocity and temperature, respectively. A detailed discussion can be found in Chapter 14 and is summarised here. Dissipation of turbulent kinetic energy in the ocean is achieved by assuming isotropy and smooth v profiles, such that

$$\epsilon = \frac{15}{2} v \left\langle \left(\frac{\partial u}{\partial z} \right) \right\rangle^2 . \tag{4.23}$$

This allows ϵ to be estimated from very fine resolution observations of velocity shear by microstructure profilers (e.g., Gregg, 1998; Ward et al., 2004), Lagrangian floats (Lien and D'Asaro, 2006), or through sophisticated analysis of acoustic Doppler measurements (Thomson et al., 2012; McCaffrey et al., 2015). Microstructure measurements in the mixed layer are generally collected by ship-based free falling profilers.

The decay of temperature variance in the ocean surface boundary layer can also be assumed under isotropy to provide an estimate of turbulence dissipation (Osborn, 1980; Oakey, 1982):

$$\epsilon = 6\kappa_T \left\langle \left(\frac{\partial T}{\partial z} \right) \right\rangle^2 . \tag{4.24}$$

High-frequency and precise measurements of fine-scale temperature gradients in the ocean are easier to obtain than velocity shear, but may be aliased by internal waves that have strong T variance but are not turbulent. An early example of this approach in the mixed layer is Oakey and Elliott (1982), and a detailed comparison versus the dissipation method is Kocsis
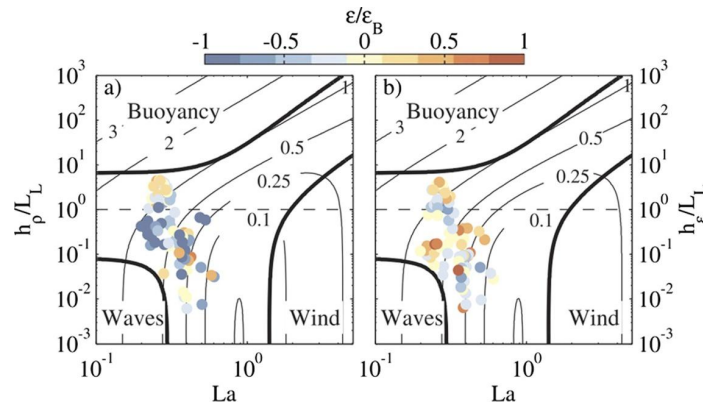
FIGURE 4.6 Values of ϵ from the North Atlantic obtained using microstructure measurements from the air-sea interaction profiler, non-dimensionalised by a dissipation scale ϵ_B (see Belcher et al. (2012) using a) mixed-layer depth h and (b) mixing-layer depth h_ϵ for the turbulent length scale, respectively. The black lines show the contours for $\log_{10}\epsilon_B$ with the heavy black lines denoting where the forcing accounts for 90% of the total dissipation. To be compared with Fig. 4.3. Reproduced with permission from Sutherland et al. (2014).

et al. (1999). Moulin et al. (2018) combined measurements of stratification of the upper 10 m with surface fluxes and turbulence measurements to show the importance of penetrating solar fluxes on turbulence suppression in diurnal warm layers, noting that penetrative solar fluxes not predicted by M–O theory play a role in upper ocean mixing (Section 4.2.2.3).

4.3.2   Wave-driven turbulence

Alongside measurements of turbulence, to assess wave-driven turbulence metrics of sea state conditions need to be collected alongside the turbulence measurements. The surface wave instrument float with tracking (SWIFT, Thomson, 2012) is an example of an instrument capturing both waves and dissipation. Surface buoys, stereo video capture (e.g., Vieira et al., 2020), X-band radar (Lund et al., 2016), radar combined with video (Benetazzo et al., 2018), or ultrasonic altimeters (Christensen et al., 2013) can all be used for wave observations.

Examples of the combined wave and turbulence observations show that the ocean surface mixed layer depends on wave state. Huang et al. (2012) observed the turbulence dissipation rate of the upper layer in the deep water of the South China sea, and compared the measurements with the non-breaking surface wave scheme and the law of wall, whereas the former fits the data well the latter is inconsistent. D'Asaro et al. (2014) collected a wide range of observations under varying sea state and wind conditions, and showed that a Langmuir turbulence scaling (Harcourt and D'Asaro, 2008) was consistent with the turbulence statistics, whereas a shear turbulence scaling was not. There are many difficulties in such measurements, since the energy density of surface waves is 3–5 orders of magnitude larger than that of boundary layer turbulence, and winds and waves often covary, because wind waves often dominate. Harcourt and D'Asaro (2008) performed experiments in the lee of a floating bridge to find calm seas in strong winds. Qiao et al. (2016) directly observed ocean velocity at a 64 Hz sampling rate under typhoon conditions and strong turbulence. Sutherland et al. (2013) compared the observed profiles of turbulent kinetic energy dissipation with different scalings and found that the non-breaking wave scheme proposed by Huang and Qiao (2010) is consistent. Sutherland et al. (2014) compared observed dissipation profiles versus scalings for Langmuir turbulence differing in whether the mixing layer or mixed layer depth is used, but again they found that wave enhancement is required for consistency with Fig. 4.3 as in Fig. 4.6 (Belcher et al., 2012). In all cases, experimental results indicate that the wave-turbulence interaction induces higher levels of background turbulence beyond the M–O theory for shear turbulence under a rigid boundary.

4.3.3   Laboratory experiments

Dai et al. (2010) designed laboratory experiments, where they cool down the bottom temperature to make a temperature stratification. It would take 20 hours to destroy the temperature stratification by molecular mixing. The stratification is destroyed within 30 minutes if non-breaking surface waves are generated in the tank. This experiment shows, as do other tank experiments (e.g., Babanin and Haus, 2009), that turbulent mixing is elevated in the presence of waves.

Similarly, there have been tank experiments claiming to set up mean flows and Stokes drift effects (e.g., Monismith et al., 2007). However, a recent important study (Calvert et al., 2019) makes it clear how difficult it is to control the production

of spurious mean flows, which when studying turbulence that is much less energetic than surface waves, such as Langmuir turbulence and non-breaking wave turbulence, is of critical importance.

4.4   Modelling surface layers and their processes

There are a variety of models of upper-ocean and lower atmosphere boundary layers. This section provides a guide to the approaches taken and highlights some recent example studies.

4.4.1   Large eddy simulations

Large eddy simulations (LES) are carried out to study both the atmospheric and oceanic boundary layers, although rarely in coupled settings of atmosphere, ocean, and waves. Instead aspects of the wavy (Sullivan et al., 2014) and heterogeneous (Sullivan et al., 2020) surface conditions have been studied.

  LES are defined by their ability to resolve partly into the 3D isotropic turbulence range, where turbulence parameterisations appropriate to that regime can be used (e.g., Sullivan et al., 1994; Fox-Kemper and Menemenlis, 2008). These simulations do not attempt to resolve the scales of molecular viscosity or diffusion, which would limit the scale of problem being considered to be many orders of magnitude smaller, but some sensitivity remains to which LES closures are chosen. Due to the relatively shallow spectral slopes of isotropic turbulence, this means that LES are not suitable for predicting vorticity or potential vorticity statistics (Bodner and Fox-Kemper, 2020). Resolving isotropic turbulence requires nonhydrostatic effects, which further constrain the choice of fluid dynamics codes away from most common ocean models.

  This chapter has emphasised the effects of surface waves on boundary layer turbulence, and LES are one key tool in that study. Early LES (Skyllingstad and Denbo, 1995; McWilliams et al., 1997) simulated the wave-averaged equations (Lane et al., 2007) or generalised Lagrangian mean theory following the theoretical framing of Craik and Leibovich (1976). Ardhuin et al. (2017) offers a wide comparison of the theoretical approaches and their degree of consistency. Theoretical work focusing on understanding and solutions of these equations (Chini and Leibovich, 2005; Chini et al., 2009; Suzuki and Fox-Kemper, 2016; Holm and Hu, 2021) have emphasised how the Stokes vortex force, or equivalently the Stokes shear force, on driving turbulent motions in the boundary layer. These forces also affect larger lateral scale balances, such as Ekman (McWilliams et al., 2012), geostrophic balance and adjustment (McWilliams and Fox-Kemper, 2013), frontogenesis and filamentogenesis (Suzuki and Fox-Kemper, 2016; Sullivan and McWilliams, 2019), and submesoscale instabilities (Haney et al., 2015). Most of these studies were triggered by examination of LES in large enough domains to have submesoscale features present (Hamlington et al., 2014).

  However, non-breaking wave theory suggests that it is not the average linkage between waves and turbulence that is important, but interaction of waves and turbulence enhances the pre-existing turbulence (Teixeira and Belcher, 2002; Babanin, 2006; Huang and Qiao, 2010). This effect is not captured fully in the wave-averaged equations, despite the high resolution of LES. LES with free surface, wave-phase-resolving physics are beginning to reveal aspects of these dynamics and whether they are importantly different from the wave-averaged theories of Langmuir turbulence (Wang and Ozgokmen, 2018; Fujiwara et al., 2018; Xuan et al., 2019). Computational limitations prevent large wave steepness and breaking in these simulations, which is one condition where the wave-averaged theory is expected to fail (Wang and Ozgokmen, 2018). Similarly, the large parameter space needing to be explored to compare different theories (Fujiwara et al., 2018) has only begun, and has not yet considered time-dependent wave trains or strongly sheared flows, where the wave-averaged theories are expected to break down. However, all of these studies find strong support for the interpretation of the wave-averaged theories as consistent with the phase-resolved vortex tilting and stretching mechanism (Teixeira and Belcher, 2002), but Xuan et al. (2019) find evidence for phase-resolved turbulent vorticity production potentially enhancing mixing *beyond what is predicted by the wave-averaged equations*.

4.4.2   1D boundary layer models

In most weather and climate applications, the lateral grid spacing of the ocean model is much wider than the boundary layer depth, so even the largest isotropic turbulence of the boundary layer cannot be resolved. Relatedly, these models are typically hydrostatic, which offers computational efficiency and little loss of accuracy when the discretisation is focused on wide, shallow features. In such simulations, all aspects of boundary layer turbulence must be parameterised, typically through providing a set of vertical fluxes based on the surface forcing and resolved profiles at each gridpoint. This 1D or "pencil" modelling approach is typically required for all realistic models.

  There is a diversity of theoretical approaches to developing 1D models, and so recent software has offered the capability to switch among the different approaches. CVmix (Griffies et al., 2015) and GOTM (Umlauf and Burchard, 2005; Umlauf

et al., 2016) offer community software to make switching between schemes easy. Recent comparison papers (Mukherjee et al., 2016; Van Roekel et al., 2018; Li et al., 2019; Dong et al., 2020) have exploited and expanded these codes to gain perspective on the ensemble span of these 1D models. Other comparison papers have also examined impacts of parameterisations without these tools (e.g., Reffray et al., 2015; Wu et al., 2015; Buckingham et al., 2019; Ali et al., 2019) or optimising parameters of the parameterisations (Souza et al., 2020).

4.4.2.1 Slab mixed layers

The simplest model of the oceanic mixed layer is the slab ocean model, which has a fixed-in-time mixed layer depth and fixed oceanic fluxes, but predicts sea surface temperature and salinity variability. This type of model is mainly used as a lower boundary condition for atmospheric models, but occasionally is used to show sensitivity of atmospheric or forecast systems to varying mixed layer depths (e.g., Samanta et al., 2018).

4.4.2.2 K-profile parameterisations

The K-profile parameterisation approach is used in both atmospheric (Troehn and Mahrt, 1986) and oceanic applications (Large et al., 1994). These 1D models specify profiles of diffusivity and viscosity following the predictions of M–O theory and other extensions (such as the free convective velocity from Section 4.2.2.2). In the ocean case, traditionally a critical Richardson number is used to find the boundary-layer depth and scale the vertical coordinate. Recent improvements on the algorithm underlying this boundary-layer depth calculation (Shchepetkin and McWilliams, 2009; Van Roekel et al., 2018) lead to surprisingly large impacts (Li et al., 2019). For this reason, numerical implementation remains important. Improvements to the physics of these schemes are many, because the underlying equations are so simply related to the M–O theory. Li et al. (2016) show that including extra wave-induced mixing based on Langmuir turbulence improves climate models. Li and Fox-Kemper (2017) shows that Langmuir-induced entrainment also improves the coupled system. Li et al. (2019) show that whereas Langmuir effects are modest on average mixed-layer properties, models without Langmuir mixing fail to reproduce LES of the wave-averaged equations.

4.4.2.3 Second-moment closures

Second-moment closure schemes build upon a closed set of prediction equations for all second moments, such as kinetic energy and fluxes, based on a simplifying assumptions, e.g., neglecting the contribution of third-moments (Umlauf and Burchard, 2005). Commonly, these schemes come in two-equation form, where two turbulent quantities (e.g., energy and length, or energy and frequency, or energy and dissipation) are solved for with PDEs in depth and time, or one-equation form, where only one such quantity is solved for (e.g., Blanke and Delecluse, 1993). These schemes have been a common choice for boundary-layer schemes in coastal modelling (Umlauf and Burchard, 2005), but in climate modelling, the coarse vertical grid scale and long-time steps tend to make them less robust. A recent development in the theory of second-moment closures is a major theoretical expansion on their treatment of Langmuir turbulence (Harcourt, 2013, 2015), including explicit treatment of the Stokes vortex force and the pressure-strain correlation, expanding the impact of wave-driven mixing beyond earlier approaches considering only the Stokes shear production (Kantha and Clayson, 2004). The non-breaking surface wave induced vertical mixing can improve the second-moment closure, and then simulation of the mixed layer in coastal ocean models (Lin et al., 2006), global ocean models (Qiao et al., 2004, 2010) and climate models (Fan and Griffies, 2014).

4.4.2.4 Bulk mixed layers

Bulk mixed layers integrate over the full mixed layer, and then close for momentum, energy (mechanical and thermal), and freshwater and salt budgets (Kraus and Turner, 1967; Niiler and Kraus, 1977; Price et al., 1986). These models have the great advantage that they are built on a solid theoretical basis of conserved properties and their relatively low level of detail provides them with robust numerical implementations over a wide range of time steps and vertical discretisations. However, because they do not provide properties in vertical profile, they are mainly used to analyse observations, and until recently they were not considered accurate enough for climate and weather modelling, However, the recent adaptation of the concept of energy constraints, but in a system using approximate vertical structures drawn from profiles second-moment schemes and LES after rescaling based on similarity theory and adapting a shear turbulence parameterisation to operate under longer-time steps (Jackson et al., 2008), has developed into the energetics-based planetary boundary layer (ePBL) scheme (Reichl and Hallberg, 2018). It shares energy conservation with bulk schemes, vertical profiles with second-moment schemes, and uses implicit numerics to allow for robust behaviour even under large time steps and grid spacings. Li et al. (2019) adapt

the Langmuir mixing enhancements applied in the K-profile parameterisation (Li et al., 2016; Li and Fox-Kemper, 2017) to ePBL.

4.4.2.5   Prognostic vs. diagnostic boundary layer depth

Each of the schemes above has a method for determining the boundary-layer depth. The K-profile parameterisation tends to have a diagnostic boundary-layer depth that is found from profiles at each time step without memory. This approach makes the scheme capable of long-time steps. The second-moment schemes tend to predict evolving boundary-layer depths, which limit their time steps and can lead to numerical instabilities and oscillations. The ePBL scheme features an implicit diagnostic boundary-layer depth calculation. The OSMOSIS scheme (prototype presented in Li et al., 2019) features a prognostic boundary-layer depth, which gives it very different behaviour from other schemes especially in reproducing variability in deepening observed at the OSMOSIS mooring array (Buckingham et al., 2019).

4.4.2.6   Non-breaking wave mixing

Many models underestimate the ocean mixed-layer depth in summer and overestimate it in winter (Fox-Kemper et al., 2011; Sallée et al., 2013; Heuzé, 2017). This may indicate that the vertical mixing in the upper ocean is too weak in summer, whereas too strong in winter. Wave breaking can generate turbulence, however this process can only affect the depth in the order of wave amplitude, i.e., within several metres, so it contributes little to mixing the whole ocean mixed layer. Qiao et al. (2004, 2010) note that surface waves may affect the ocean on the order of their wave length ($\approx$100 m), which coincides with the ocean mixed layer—deeper than the summertime depth and shallower than the wintertime—and were inspired to introduce a non-breaking wave-induced mixing theory (Bv theory). This theory relates enhanced turbulence to the scales of the waves orbital motion, and therefore provides more energy for mixing when waves are strong within the upper ocean, where orbital velocities are large. The Bv has been tested by different groups with different ocean circulation models; most models showed improvement in the simulation of the ocean mixed layer, such as in a lake model (Torma and Krámer, 2017), 2016, 1D models (Ghantous and Babanin, 2014; Wu et al., 2015), the coastal Princeton ocean model (Lin et al., 2006), a global instance of the AWI ocean model (Wang et al., 2019b), and other climate models (Qiao et al., 2013; Bao et al., 2020), which suggest that the physics represented by Bv are missing in many models. Fan and Griffies (2014) found that the Bv scheme mixed too much, as did some other schemes (McWilliams and Sullivan, 2000), but after limiting its effects below 100 m, they found that it deepened summertime mixed layers more effectively than the other schemes tested, which is a common challenge for nearly all ocean circulation models and climate models (Sallée et al., 2013). Bv can shoal the ocean mixed-layer simulation in winter (Chen et al., 2019) by transferring more heat to subsurface, and so enhance the ocean stratification in winter, resulting in a shallower mixed layer in winter.

The Bv scheme produces additional vertical viscosity and diffusivity where waves are strong and more deeply when waves are long. This additional viscosity is added into the other sources in the model's parameterisation (Qiao et al., 2010). The Langmuir schemes described above and reviewed and compared in (Li et al., 2019) also mix more where waves are strong and more deeply when wavelengths are long. These schemes thus differ only in their theoretical framing and their quantitative aspects, which makes it very difficult to use bias reduction as a discriminant. Indeed, as mentioned above, both theories rely on the heuristic of tilting and stretching of turbulent vorticity by passing waves (Teixeira and Belcher, 2002), but differ in whether or not these effects can be captured in wave-averaged equations, or if phase-locked phenomena go beyond the wave-averaged contributions. To conclude, a comparison of Langmuir 1D schemes and non-breaking schemes, such as the Bv scheme need to be compared against wave-phase-resolving simulations under a wide range of realistic conditions to better understand the flaws and oversimplifications in each approach.

4.4.3   Ocean and climate models

The previous section discusses a variety of new 1D parameterisations, but of course these parameterisations are developed to improve 3D ocean and climate modelling systems. Many of the new breakthroughs require wave information, which is often modelled as a new coupled system component: MASNUM in Qiao et al. (2010, 2013); Bao et al. (2020), WaveWatch-III in (Li et al., 2016, 2017), and WAM in ECMWF atmosphere-wave coupled system, which only alters air-sea fluxes not ocean mixing (Bidlot et al., 2007). The additional cost of adding the wave models can be considerable, and so statistical approaches have been attempted. For some applications, such as predicting Langmuir mixing, they are adequately accurate (Li et al., 2017). For more advanced purposes, such as interactions of waves and sea ice, future developments toward efficiency are needed (Roach et al., 2018).

A new earth system model (FIO-ESMv2.0) was developed by including four processes, including the non-breaking surface wave-induced mixing (Bv), sea spray from wave breaking, and the effects of Stokes drift in air-sea fluxes and the

diurnal cycle of sea surface temperature. The mixed-layer depth in the upper ocean and historical sea surface temperature during 1850–2014 are well reproduced (Bao et al., 2020). For the CMIP5 generation of coupled models, only the FIO model included wave effects, and this FIO model is also part of the CMIP6 ensemble along with a few other models, including wave effects (e.g., CESM, Li et al., 2016).

Other models in the CMIP6 ensemble have had improvements in their boundary-layer schemes as well. The CESM now has a K-profile parameterisation, including Langmuir mixing, which improves summer and winter mixed-layer depths in the extratropical oceans and subsurface ventilation and temperatures (Li et al., 2016; Danabasoglu et al., 2020). The GFDL CM4.0 has ePBL (Reichl and Hallberg, 2018) as its boundary-layer scheme, brings strong improvement to Southern ocean summer and winter mixed-layer depths and temperatures (Dunne et al., 2020).

4.5 Global perspective

4.5.1 Energy and forcing

The ocean surface boundary layer is forced by winds, waves, and convection, which are partly represented in Fig. 4.3. This forcing, when combined with ocean currents and other feedbacks, leads to the patterns of mixed-layer depth and stratification observed and modelled, Figs. 4.4–4.5. Elimination of large-scale vertical shear in the surface boundary layer is the largest sink of kinetic energy in models (Fig. 4.1). Through the energy budget (4.19), geographical variation of ocean boundary-layer properties, forcing and turbulence is how potential energy enters the ocean (Fig. 4.4).

These layers respond to energetic forcing and also have the ability to shape it. As already noted, the phenomenon of surface cooling, with deeper warming by radiation, is the only solar heat engine in the ocean (Fig. 4.2).

4.5.2 Surface layers, weather, and climate

Since Hasselmann (1976), the ocean surface boundary layer has been considered an important agent of calming the weather and thereby creating a climate. The air-sea fluxes discussed here, and especially the entrainment and connections to the deeper ocean, are part of how this long-term climate variability occurs.

Goswami et al. (2016) and Orenstein (2018) are two good examples of how air-sea coupling affects not only the ocean but also the atmosphere through coupled modes of variability—in this case, intraseasonal variability of the Indian monsoon. These studies show observationally and through perturbed physics models that features in the upper ocean of the Bay of Bengal are associated with monsoon variability (and thus with societally important rainfall predictions).

The ocean surface boundary layers are also important for climate. This result is often shown by climate model sensitivity to perturbed physics (e.g., Danabasoglu and Gent, 2009), but a deeper connection to how our planet works has emerged as well. Many studies have begun to simplify the ocean's role in the planetary energy balance as a reservoir of energy, specifically akin to a simple two-layer model (Gregory, 2000; Gregory et al., 2004; Gregory and Forster, 2008; Geoffroy et al., 2013b,a; Held et al., 2010; Winton et al., 2010; Hall and Fox-Kemper, 2021). The upper layer of this model connects to both the atmosphere and the deep ocean, and this deep ocean connection has been shown to link to Atlantic meridional overturning (Kostov et al., 2014). However, a recent student project reveals intriguing connections between the dynamics of the mixed layer (dynamically defined as in this chapter) and the upper layer and upper to lower-layer connectivity in these simplified climate models (Hall, 2020). His results indicate that the mixed layer is an observable emergent phenomenon that constrains many properties of the climate sensitivity to forcing—natural and anthropogenic—on decadal to centennial timescales (Hall and Fox-Kemper, 2021). Continued study of the mixed layer and its dynamics are a crucial part of modelling the earth's weather and climate.

4.6 Outlook

As our understanding of the ocean surface layers (and the closely related atmospheric surface layers) has evolved, the M–O approach has served as a useful guide. However, as this chapter has noted, a variety of topics of present interest require approaches that go beyond the M–O theory: waves (Bv, Langmuir, breaking, spray, etc.), submesoscales, penetrating radiation, sea ice, and spatiotemporal variability in forcing. A variety of observational approaches and modelling practice have developed to establish "sea truth," and the treatment and impacts of these phenomena beyond M–O in weather and climate models. However, it remains challenging to perform comparative analysis and synthesis of these different approaches, although recent examples utilising community software (Umlauf and Burchard, 2005; Li et al., 2019), regimes of behaviour (Belcher et al., 2012), and evaluation of scalings (Sutherland et al., 2013, 2014) exemplify potential paths forward. Nu-

merical sensitivity and model development experiments show great potential for model bias reduction through continued surface layer improvements.

Acknowledgements

References

Alford, M.H., MacKinnon, J.A., Simmons, H.L., Nash, J.D., 2016. Near-inertial internal gravity waves in the ocean. Annu. Rev. Mar. Sci. 8, 95–123. https://doi.org/10.1146/annurev-marine-010814-015746.

Ali, A., Christensen, K.H., Breivik, Ø., Malila, M., Raj, R.P., Bertino, L., et al., 2019. A comparison of Langmuir turbulence parameterizations and key wave effects in a numerical model of the North Atlantic and Arctic oceans. Ocean Model. 137, 76–97. https://doi.org/10.1016/j.ocemod.2019.02.005.

Ardhuin, F., Suzuki, N., McWilliams, J.C., Aiki, H., 2017. Comments on "a combined derivation of the integrated and vertically resolved, coupled wave-current equations". J. Phys. Oceanogr. 47 (9), 2377–2385. https://doi.org/10.1175/JPO-D-17-0065.1.

Babanin, A., 2006. On a wave-induced turbulence and a wave-mixed upper ocean layer. Geophys. Res. Lett. 33, L20605. https://doi.org/10.1029/2006GL027308.

Babanin, A.V., Haus, B.K., 2009. On the existence of water turbulence induced by nonbreaking surface waves. J. Phys. Oceanogr. 39 (10), 2675–2679. https://doi.org/10.1175/2009JPO4202.1.

Bachman, S.D., Fox-Kemper, B., Taylor, J.R., Thomas, L.N., 2017. Parameterization of frontal symmetric instabilities. I: theory for resolved fronts. Ocean Model. 109, 72–95. https://doi.org/10.1016/j.ocemod.2016.12.003.

Bao, Y., Song, Z., Qiao, F., 2020. FIO-ESM version 2.0: model description and evaluation. J. Geophys. Res., Oceans 125 (6), e2019JC016036. https://doi.org/10.1029/2019JC016036.

Baumert, H.Z., Simpson, J., Simpson, J.H., Sundermann, J., Sündermann, J., 2005. Marine Turbulence: Theories, Observations, and Models. Cambridge University Press.

Belcher, S.E., Grant, A.A.L.M., Hanley, K.E., Fox-Kemper, B., Van Roekel, L., Sullivan, P.P., et al., 2012. A global perspective on Langmuir turbulence in the ocean surface boundary layer. Geophys. Res. Lett. 39 (18), L18605. https://doi.org/10.1029/2012GL052932.

Benetazzo, A., Serafino, F., Bergamasco, F., Ludeno, G., Ardhuin, F., Sutherland, P., et al., 2018. Stereo imaging and X-band radar wave data fusion: an assessment. Ocean Eng. 152, 346–352. https://doi.org/10.1016/j.oceaneng.2018.01.077.

Bidlot, J., Janssen, P., Abdalla, S., Hersbach, H., 2007. A Revised Formulation of Ocean Wave Dissipation and Its Model Impact. ECMWF, Reading, UK.

Blanke, B., Delecluse, P., 1993. Variability of the tropical Atlantic Ocean simulated by a general circulation model with two different mixed-layer physics. J. Phys. Oceanogr. 23 (7), 1363–1388.

Boccaletti, G., Ferrari, R., Fox-Kemper, B., 2007. Mixed layer instabilities and restratification. J. Phys. Oceanogr. 37 (9), 2228–2250. https://doi.org/10.1175/JPO3101.1.

Bodner, A., Fox-Kemper, B., 2020. A breakdown in potential vorticity estimation delineates the submesoscale-to-turbulence boundary in large eddy simulations. J. Adv. Model. Earth Syst. 12 (10), e2020MS002049. https://doi.org/10.1029/2020MS002049.

Bodner, A., Fox-Kemper, B., Van Roekel, L., McWilliams, J., Sullivan, P., 2020. A perturbation approach to understanding the effects of turbulence on frontogenesis. J. Fluid Mech. 883, A25. https://doi.org/10.1017/jfm.2019.804.

Brunner, K., Kukulka, T., Proskurowski, G., Law, K.L., 2015. Passive buoyant tracers in the ocean surface boundary layer: 2. observations and simulations of microplastic marine debris. J. Geophys. Res., Oceans 120 (11), 7559–7573. https://doi.org/10.1002/2015JC010840.

Buckingham, C.E., Lucas, N.S., Belcher, S.E., Rippeth, T.P., Grant, A.L.M., Sommer, J.L., et al., 2019. The contribution of surface and submesoscale processes to turbulence in the open ocean surface boundary layer. J. Adv. Model. Earth Syst. 11 (12), 4066–4094. https://doi.org/10.1029/2019MS001801.

Calvert, R., Whittaker, C., Raby, A., Taylor, P., Borthwick, A., Van Den Bremer, T., 2019. Laboratory study of the wave-induced mean flow and set-down in unidirectional surface gravity wave packets on finite water depth. Phys. Rev. Fluids 4 (11), 114801. https://doi.org/10.1103/PhysRevFluids.4.114801.

Cavaleri, L., Bertotti, L., Bidlot, J.-R., 2015. Waving in the rain. J. Geophys. Res., Oceans 120 (5), 3248–3260. https://doi.org/10.1002/2014JC010348.

Cavaleri, L., Fox-Kemper, B., Hemer, M., 2012. Wind waves in the coupled climate system. Bull. Am. Meteorol. Soc. 93 (11), 1651–1661. https://doi.org/10.1175/BAMS-D-11-00170.1.

Chang, H., Huntley, H.S., Kirwan Jr., A.D., Carlson, D.F., Mensa, J.A., Mehta, S., et al., 2019. Small-scale dispersion in the presence of Langmuir circulation. J. Phys. Oceanogr. 49 (12), 3069–3085. https://doi.org/10.1175/JPO-D-19-0107.1.

Charnock, H., 1955. Wind stress on a water surface. Q. J. R. Meteorol. Soc. 81, 639. https://doi.org/10.1002/qj.49708135027.

Chassignet, E.P., Yeager, S., Fox-Kemper, B., Bozec, A., Castruccio, F., Danabasoglu, G., et al., 2020. Impact of horizontal resolution on global ocean-sea-ice model simulations based on the experimental protocols of the Ocean Model Intercomparison Project phase 2 (OMIP-2). Geosci. Model Dev. 13. https://doi.org/10.5194/gmd-13-4595-2020.

Chen, S., Qiao, F., Huang, C.J., Zhao, B., 2018. Deviation of wind stress from wind direction under low wind conditions. J. Geophys. Res., Oceans 123. https://doi.org/10.1029/2018JC014137.

Chen, S., Qiao, F., Jiang, W., Guo, J., Dai, D., 2019. Impact of surface waves on wind stress under low to moderate wind conditions. J. Phys. Oceanogr. 49 (8), 2017–2028. https://doi.org/10.1175/JPO-D-18-0266.1.

Chini, G., Leibovich, S., 2005. Resonant Langmuir-circulation-internal-wave interaction. Part 2. Langmuir circulation instability. J. Fluid Mech. 524, 99–120. https://doi.org/10.1017/S002211200400182X.

Chini, G.P., Julien, K., Knobloch, E., 2009. An asymptotically reduced model of turbulent Langmuir circulation. Geophys. Astrophys. Fluid Dyn. 103 (2), 179–197. https://doi.org/10.1080/03091920802622236.

Choy, C.A., Robison, B.H., Gagne, T.O., Erwin, B., Firl, E., Halden, R.U., et al., 2019. The vertical distribution and biological transport of marine microplastics across the epipelagic and mesopelagic water column. Sci. Rep. 9 (1), 1–9. https://doi.org/10.1038/s41598-019-44117-2.

Christensen, K.H., Röhrs, J., Ward, B., Fer, I., Broström, G., Saetra, Ø., Breivik, Ø., 2013. Surface wave measurements using a ship-mounted ultrasonic altimeter. Methods Oceanogr. 6, 1–15. https://doi.org/10.1016/j.mio.2013.07.002.

Codiga, D.L., Ullman, D.S., 2010. Characterizing the physical oceanography of coastal waters off Rhode Island, Part 1: literature review, available observations, and a representative model simulation. In: Appendix to Rhode Island Ocean Special Area Management Plan, pp. 1–170.

Craik, A.D.D., Leibovich, S., 1976. Rational model for Langmuir circulations. J. Fluid Mech. 73, 401–426. https://doi.org/10.1017/S0022112076001420.

Cronin, M.F., Gentemann, C.L., Edson, J.B., Ueki, I., Bourassa, M., Brown, S., et al., 2019. Air-sea fluxes with a focus on heat and momentum. Front. Mar. Sci. 6, 430. https://doi.org/10.3389/fmars.2019.00430.

Crowe, M.N., Taylor, J.R., 2018. The evolution of a front in turbulent thermal wind balance. Part 1. Theory. J. Fluid Mech. 850, 179–211. https://doi.org/10.1017/jfm.2018.448.

Csanady, G.T., 2000. Air-Sea Interaction. Cambridge University Press, New York.

Dai, D., Qiao, F., Sulisz, W., Han, L., Babanin, A., 2010. An experiment on the nonbreaking surface-wave-induced vertical mixing. J. Phys. Oceanogr. 40 (9), 2180–2188. https://doi.org/10.1175/2010JPO4378.1.

Dale, A.C., Barth, J.A., Levine, M.D., Austin, J.A., 2008. Observations of mixed layer restratification by onshore surface transport following wind reversal in a coastal upwelling region. J. Geophys. Res. 113 (C1), C01010. https://doi.org/10.1029/2007JC004128. http://doi.wiley.com/10.1029/2007JC004128.

Danabasoglu, G., Ferrari, R., McWilliams, J.C., 2008. Sensitivity of an ocean general circulation model to a parameterization of near-surface eddy fluxes. J. Climate 21 (6), 1192–1208. https://doi.org/10.1175/2007JCLI1508.1.

Danabasoglu, G., Gent, P.R., 2009. Equilibrium climate sensitivity: is it accurate to use a slab ocean model? J. Climate 22 (9), 2494–2499. https://doi.org/10.1175/2008JCLI2596.1.

Danabasoglu, G., Lamarque, J.-F., Bacmeister, J., Bailey, D.A., DuVivier, A.K., Edwards, J., et al., 2020. The Community Earth System Model version 2 (CESM2). J. Adv. Model. Earth Syst. 12 (2), e2019MS001916. https://doi.org/10.1029/2019MS001916.

D'Asaro, E.A., 2003. The ocean boundary layer below Hurricane Dennis. J. Phys. Oceanogr. 33 (3), 561–579.

D'Asaro, E.A., 2014. Turbulence in the upper-ocean mixed layer. Annu. Rev. Mar. Sci. 6, 101–115. https://doi.org/10.1146/annurev-marine-010213-135138.

D'Asaro, E.A., Shcherbina, A.Y., Klymak, J.M., Molemaker, J., Novelli, G., Guigand, C.M., et al., 2018. Ocean convergence and the dispersion of flotsam. Proc. Natl. Acad. Sci. 115 (6), 1162–1167. https://doi.org/10.1073/pnas.1718453115.

D'Asaro, E.A., Thomson, J., Shcherbina, A.Y., Harcourt, R.R., Cronin, M.F., Hemer, M.A., Fox-Kemper, B., 2014. Quantifying upper ocean turbulence driven by surface waves. Geophys. Res. Lett. 41 (1), 102–107. https://doi.org/10.1002/2013GL058193.

Dauhajre, D.P., McWilliams, J.C., 2018. Diurnal evolution of submesoscale front and filament circulations. J. Phys. Oceanogr. 48 (10), 2343–2361. https://doi.org/10.1175/JPO-D-18-0143.1.

de Boyer Montégut, C., Madec, G., Fischer, A.S., Lazar, A., Iudicone, D., 2004. Mixed layer depth over the global ocean: an examination of profile data and a profile-based climatology. J. Geophys. Res., Oceans 109, C12. https://doi.org/10.1029/2004JC002378.

Dong, J., Fox-Kemper, B., Zhang, H., Dong, C., 2020. The scale of submesoscale baroclinic instability globally. J. Phys. Oceanogr. 50 (9), 2649–2667. https://doi.org/10.1175/JPO-D-20-0043.1.

Dong, J., Fox-Kemper, B., Zhang, H., Dong, C., 2021. The scale and activity of symmetric instability globally. J. Phys. Oceanogr. 51 (5), 1655–1670. https://doi.org/10.1175/JPO-D-20-0159.1.

Dunne, J., Horowitz, L., Adcroft, A., Ginoux, P., Held, I., John, J., et al., 2020. The GFDL Earth System Model Version 4.1 (GFDL-ESM 4.1): Overall coupled model description and simulation characteristics. J. Adv. Model. Earth Syst., e2019MS002015. https://doi.org/10.1029/2019MS002015.

Edson, J., Crawford, T., Crescenti, J., Farrar, T., Frew, N., Gerbi, G., et al., 2007. The coupled boundary layers and air-sea transfer experiment in low winds. Bull. Am. Meteorol. Soc. 88 (3), 341. https://doi.org/10.1175/BAMS-88-3-341.

Fairall, C.W., Bradley, E.F., Rogers, D.P., Edson, J.B., Young, G.S., 1996. Bulk parameterization of air-sea fluxes for Tropical Ocean-Global Atmosphere Coupled-Ocean Atmosphere Response Experiment. J. Geophys. Res., Oceans 101, 3747–3764. https://doi.org/10.1029/95JC03205.

Fan, Y., Griffies, S.M., 2014. Impacts of parameterized Langmuir turbulence and nonbreaking wave mixing in global climate simulations. J. Climate 27 (12), 4752–4775. https://doi.org/10.1175/JCLI-D-13-00583.1.

Ferrari, R., Paparella, F., 2003. Compensation and alignment of thermohaline gradients in the ocean mixed layer. J. Phys. Oceanogr. 33 (11), 2214–2223.

Fox-Kemper, B., Danabasoglu, G., Ferrari, R., Griffies, S.M., Hallberg, R.W., Holland, M.M., et al., 2011. Parameterization of mixed layer eddies. III: implementation and impact in global ocean climate simulations. Ocean Model. 39, 61–78. https://doi.org/10.1016/j.ocemod.2010.09.002.

Fox-Kemper, B., Ferrari, R., Hallberg, R.W., 2008. Parameterization of mixed layer eddies. Part I: theory and diagnosis. J. Phys. Oceanogr. 38 (6), 1145–1165. https://doi.org/10.1175/2007JPO3792.1.

Fox-Kemper, B., Menemenlis, D., 2008. Can large eddy simulation techniques improve mesoscale-rich ocean models? In: Hecht, M., Hasumi, H. (Eds.), Ocean Modeling in an Eddying Regime, Vol. 177. In: AGU Geophysical Monograph Series, pp. 319–338.

Fujiwara, Y., Yoshikawa, Y., Matsumura, Y., 2018. A wave-resolving simulation of Langmuir circulations with a nonhydrostatic free-surface model: comparison with Craik–Leibovich theory and an alternative Eulerian view of the driving mechanism. J. Phys. Oceanogr. 48 (8), 1691–1708. https://doi.org/10.1175/JPO-D-17-0199.1.

Gargett, A., Wells, J., Tejada-Martinez, A., Grosch, C., 2004. Langmuir supercells: a mechanism for sediment resuspension and transport in shallow seas. Science 306 (5703), 1925–1928. https://doi.org/10.1126/science.1100849.

Gentemann, C.L., Scott, J.P., Mazzini, P.L.F., Pianca, C., Akella, S., Minnett, P.J., et al., 2020. Saildrone: adaptively sampling the marine environment. Bull. Am. Meteorol. Soc. 101 (6), E744–E762. https://doi.org/10.1175/BAMS-D-19-0015.1.

Geoffroy, O., Saint-Martin, D., Bellon, G., Voldoire, A., Olivié, D., Tytéca, S., 2013a. Transient climate response in a two-layer energy-balance model. Part II: Representation of the efficacy of deep-ocean heat uptake and validation for CMIP5 AOGCMs. J. Climate 26 (6), 1859–1876. https://doi.org/10.1175/JCLI-D-12-00196.1.

Geoffroy, O., Saint-Martin, D., Olivié, D.J., Voldoire, A., Bellon, G., Tytéca, S., 2013b. Transient climate response in a two-layer energy-balance model. Part I: Analytical solution and parameter calibration using CMIP5 AOGCM experiments. J. Climate 26 (6), 1841–1857. https://doi.org/10.1175/JCLI-D-12-00195.1.

Ghantous, M., Babanin, A., 2014. One-dimensional modelling of upper ocean mixing by turbulence due to wave orbital motion. Nonlinear Process. Geophys. 21 (1), 325–338. https://doi.org/10.5194/npg-21-325-2014.

Goswami, B., Rao, S.A., Sengupta, D., Chakravorty, S., 2016. Monsoons to mixing in the Bay of Bengal: multiscale air-sea interactions and monsoon predictability. Oceanography 29 (2), 18–27. https://www.jstor.org/stable/24862666.

Grant, A.L.M., Belcher, S.E., 2009. Characteristics of Langmuir turbulence in the ocean mixed layer. J. Phys. Oceanogr. 39 (8), 1871–1887. https://doi.org/10.1175/2009JPO4119.1.

Gregg, M.C., 1998. Estimation and geography of diapycnal mixing in the stratified ocean. Coast. Estuar. Stud. 54, 305–338. https://doi.org/10.1029/CE054p0305.

Gregory, J., Forster, P., 2008. Transient climate response estimated from radiative forcing and observed temperature change. J. Geophys. Res., Atmos. 113 (D23). https://doi.org/10.1029/2008JD010405.

Gregory, J.M., 2000. Vertical heat transports in the ocean and their effect on time-dependent climate change. Clim. Dyn. 16 (7), 501–515. https://doi.org/10.1007/s003820000059.

Gregory, J.M., Ingram, W., Palmer, M., Jones, G., Stott, P., Thorpe, R., et al., 2004. A new method for diagnosing radiative forcing and climate sensitivity. Geophys. Res. Lett. 31 (3). https://doi.org/10.1029/2003GL018747.

Griffies, S.M., Levy, M., Adcroft, A.J., Danabasoglu, G., Hallberg, R.W., Jacobsen, D., et al., 2015. Theory and numerics of the Community Ocean Vertical Mixing (CVMix) Project. Tech. Rep.. Geophysical Fluid Dynamics Laboratory, National Center for Atmospheric Research, and Los Alamos National Laboratory. https://github.com/CVMix/CVMix-description.

Hall, G., 2020. Investigating the impacts of mixed layer depth on climate sensitivity. ScB thesis. Physics, Brown University. http://www.geo.brown.edu/research/Fox-Kemper/pubs/pdfs/HallThesis.pdf.

Hall, G., Fox-Kemper, B., 2021. Regional mixed layer depth as a climate diagnostic and emergent constraint. In preparation.

Hall, T.M., Haine, T.W.N., 2002. On ocean transport diagnostics: The idealized age tracer and the age spectrum. J. Phys. Oceanogr. 32 (6), 1987–1991. https://doi.org/10.1175/1520-0485(2002)032<1987:OOTDTI>2.0.CO;2.

Hamlington, P.E., Van Roekel, L.P., Fox-Kemper, B., Julien, K., Chini, G.P., 2014. Langmuir-submesoscale interactions: descriptive analysis of multiscale frontal spin-down simulations. J. Phys. Oceanogr. 44 (9), 2249–2272. https://doi.org/10.1175/JPO-D-13-0139.1.

Haney, S., Bachman, S., Cooper, B., Kupper, S., McCaffrey, K., Van Roekel, L., et al., 2012. Hurricane wake restratification rates of 1, 2 and 3-dimensional processes. J. Mar. Res. 70 (6), 824–850. https://doi.org/10.1357/002224012806770937.

Haney, S., Fox-Kemper, B., Julien, K., Webb, A., 2015. Symmetric and geostrophic instabilities in the wave-forced ocean mixed layer. J. Phys. Oceanogr. 45, 3033–3056. https://doi.org/10.1175/JPO-D-15-0044.1.

Hanley, K.E., Belcher, S.E., Sullivan, P.P., 2010. A global climatology of wind-wave interaction. J. Phys. Oceanogr. 40 (6), 1263–1282. https://doi.org/10.1175/2010JPO4377.1.

Harcourt, R., Steffen, E., Garwood, R., D'Asaro, E., 2002. Fully Lagrangian floats in Labrador Sea deep convection: Comparison of numerical and experimental results. J. Phys. Oceanogr. 32 (2), 493–510. https://doi.org/10.1175/1520-0485(2002)032<0493:FLFILS>2.0.CO;2.

Harcourt, R.R., 2013. A second-moment closure model of Langmuir turbulence. J. Phys. Oceanogr. 43 (4), 673–697. https://doi.org/10.1175/JPO-D-12-0105.1.

Harcourt, R.R., 2015. An improved second-moment closure model of Langmuir turbulence. J. Phys. Oceanogr. 45 (1), 84–103. https://doi.org/10.1175/JPO-D-14-0046.1.

Harcourt, R.R., D'Asaro, E.A., 2008. Large-eddy simulation of Langmuir turbulence in pure wind seas. J. Phys. Oceanogr. 38 (7), 1542–1562. https://doi.org/10.1175/2007JPO3842.1.

Hasselmann, K., 1976. Stochastic climate models. Part I. Theory. Tellus 28, 473–485. https://doi.org/10.3402/tellusa.v28i6.11316.

Held, I.M., Winton, M., Takahashi, K., Delworth, T., Zeng, F., Vallis, G.K., 2010. Probing the fast and slow components of global warming by returning abruptly to preindustrial forcing. J. Climate 23 (9), 2418–2427. https://doi.org/10.1175/2009JCLI3466.1.

Heuzé, C., 2017. North Atlantic Deep Water formation and AMOC in CMIP5 models. Ocean. Sci. 13 (4), 609–622. https://doi.org/10.5194/os-13-609-2017.

Högström, U., 1996. Review of some basic characteristics of the atmospheric surface layer. Bound.-Layer Meteorol. 78 (3), 215–246. https://doi.org/10.1007/BF00120937.

Holm, D., 1996. The ideal Craik-Leibovich equations. Physica D 98 (2–4), 415–441. https://doi.org/10.1016/0167-2789(96)00105-4.

Holm, D.D., Hu, R., 2021. Stochastic effects of waves on currents in the ocean mixed layer. J. Math. Phys. 62, 073102. https://doi.org/10.1063/5.0045010.

Holte, J., Talley, L.D., Gilson, J., Roemmich, D., 2017. An Argo mixed layer climatology and database. Geophys. Res. Lett. 44 (11), 5618–5626. https://doi.org/10.1002/2017GL073426.

Holtslag, A.A., Nieuwstadt, F.T., 1986. Scaling the atmospheric boundary layer. Bound.-Layer Meteorol. 36 (1–2), 201–209. https://doi.org/10.1007/BF00117468.

Horvat, C., Tziperman, E., Campin, J.-M., 2016. Interaction of sea ice floe size, ocean eddies, and sea ice melting. Geophys. Res. Lett. 43 (15), 8083–8090. https://doi.org/10.1002/2016GL069742.

Hosegood, P., Gregg, M.C., Alford, M.H., 2006. Sub-mesoscale lateral density structure in the oceanic surface mixed layer. Geophys. Res. Lett. 33 (22), L22604. https://doi.org/10.1029/2006GL026797.

Huang, C.J., Qiao, F., 2010. Wave-turbulence interaction and its induced mixing in the upper ocean. J. Geophys. Res., Oceans 115 (C4). https://doi.org/10.1029/2009JC005853.

Huang, C.J., Qiao, F., 2021. Simultaneous observations of turbulent Reynolds stress in the ocean surface boundary layer and wind stress over the sea surface. J. Geophys. Res., Oceans, e2020JC016839. https://doi.org/10.1029/2020JC016839.

Huang, C.J., Qiao, F., Dai, D., Ma, H., Guo, J., 2012. Field measurement of upper ocean turbulence dissipation associated with wave-turbulence interaction in the South China Sea. J. Geophys. Res., Oceans 117 (C11). https://doi.org/10.1029/2011JC007806.

Huang, N.E., Hu, K., Yang, A.C., Chang, H.-C., Jia, D., Liang, W.-K., et al., 2016. On Holo-Hilbert spectral analysis: A full informational spectral representation for nonlinear and non-stationary data. Philos. Trans. R. Soc. A, Math. Phys. Eng. Sci. 374 (2065), 20150206. https://doi.org/10.1098/rsta.2015.0206.

Huang, P.-Q., Cen, X.-R., Lu, Y.-Z., Guo, S.-X., Zhou, S.-Q., 2018. An integrated method for determining the oceanic bottom mixed layer thickness based on woce potential temperature profiles. J. Atmos. Ocean. Technol. 35 (11), 2289–2301. https://doi.org/10.1175/JTECH-D-18-0016.1.

Hughes, K.G., Moum, J.N., Shroyer, E.L., 2020. Heat transport through diurnal warm layers. J. Phys. Oceanogr. 50 (1), 2885–2905. https://doi.org/10.1175/JPO-D-20-0079.1.

Jackson, L., Hallberg, R., Legg, S., 2008. A parameterization of shear-driven turbulence for ocean climate models. J. Phys. Oceanogr. 38 (5), 1033–1053. https://doi.org/10.1175/2007JPO3779.1.

Janssen, P.A., 2012. Ocean wave effects on the daily cycle in SST. J. Geophys. Res., Oceans 117 (C11). https://doi.org/10.1029/2012JC007943.

Javaid, M.Y., Ovinis, M., Nagarajan, T., Hashim, F.B., 2014. Underwater gliders: a review. In: Matec Web of Conferences, Vol.13, p. 02020.

Jing, Z., Qi, Y., Fox-Kemper, B., Du, Y., Lian, S., 2016. Seasonal thermal fronts on the northern South China Sea shelf: satellite measurements and three repeated field surveys. J. Geophys. Res., Oceans 121 (3), 1914–1930. https://doi.org/10.1002/2015JC011222.

Jochum, M., Briegleb, B.P., Danabasoglu, G., Large, W.G., Norton, N.J., Jayne, S.R., et al., 2013. The impact of oceanic near-inertial waves on climate. J. Climate 26 (9), 2833–2844. https://doi.org/10.1175/JCLI-D-12-00181.1.

Johnson, L., Fox-Kemper, B., Li, Q., Pham, H., Sarkar, S., 2021. A dynamical systems approach to mixed layer model comparison. In preparation.

Johnson, L., Lee, C.M., D'Asaro, E.A., Wenegrat, J.O., Thomas, L.N., 2020. Restratification at a California current upwelling front. Part II: Dynamics. J. Phys. Oceanogr. 50 (5), 1473–1487. https://doi.org/10.1175/JPO-D-19-0204.1.

Johnston, T.S., Rudnick, D.L., 2009. Observations of the transition layer. J. Phys. Oceanogr. 39 (3), 780–797. https://doi.org/10.1175/2008JPO3824.1.

Jones, C., Abernathey, R.P., 2019. Isopycnal mixing controls deep ocean ventilation. Geophys. Res. Lett. 46 (22), 13144–13151. https://doi.org/10.1029/2019GL085208.

Kantha, L., Clayson, C., 2004. On the effect of surface gravity waves on mixing in the oceanic mixed layer. Ocean Model. 6 (2), 101–124. https://doi.org/10.1016/S1463-5003(02)00062-8.

Kocsis, O., Prandke, H., Stips, A., Simon, A., Wüest, A., 1999. Comparison of dissipation of turbulent kinetic energy determined from shear and temperature microstructure. J. Mar. Syst. 21, 67–84. https://doi.org/10.1016/S0924-7963(99)00006-8.

Kostov, Y., Armour, K.C., Marshall, J., 2014. Impact of the Atlantic Meridional Overturning Circulation on ocean heat storage and transient climate change. Geophys. Res. Lett. 41 (6), 2108–2116. https://doi.org/10.1002/2013GL058998.

Kraus, E., Turner, J., 1967. A one-dimensional model of the seasonal thermocline. II: The general theory and its consequences. Tellus 19, 98–106. https://doi.org/10.3402/tellusa.v19i1.9753.

Lane, E.M., Restrepo, J.M., McWilliams, J.C., 2007. Wave-current interaction: a comparison of radiation-stress and vortex-force representations. J. Phys. Oceanogr. 37 (5), 1122–1141. https://doi.org/10.1175/JPO3043.1.

Large, W.G., Crawford, G.B., 1995. Observations and simulations of upper-ocean response to wind events during the Ocean Storms Experiment. J. Phys. Oceanogr. 25. https://doi.org/10.1175/1520-0485(1995)025<2831:OASOUO>2.0.CO;2.

Large, W.G., McWilliams, J.C., Doney, S.C., 1994. Oceanic vertical mixing - a review and a model with a nonlocal boundary-layer parameterization. Rev. Geophys. 32 (4), 363–403. https://doi.org/10.1029/94RG01872.

Large, W.G., Patton, E.G., DuVivier, A.K., Sullivan, P.P., Romero, L., 2019. Similarity theory in the surface layer of large-eddy simulations of the wind-, wave-, and buoyancy-forced Southern Ocean. J. Phys. Oceanogr. 49 (8), 2165–2187. https://doi.org/10.1175/JPO-D-18-0066.1.

Large, W.G., Pond, S., 1981. Open ocean momentum flux measurements in moderate to strong winds. J. Phys. Oceanogr. 11 (3), 324–336. https://doi.org/10.1175/1520-0485(1981)011<0324:OOMFMI>2.0.CO;2.

Large, W.G., Pond, S., 1982. Sensible and latent heat flux measurements over the ocean. J. Phys. Oceanogr. 12 (5), 464–482. https://doi.org/10.1175/1520-0485(1982)012<0464:SALHFM>2.0.CO;2.

Large, W.G., Yeager, S.G., 2004. Diurnal to Decadal Global Forcing for Ocean and Sea-Ice Models: The Data Sets and Flux Climatologies. National Center for Atmospheric Research Boulder.

Large, W.G., Yeager, S.G., 2009. The global climatology of an interannually varying air–sea flux data set. Clim. Dyn. 33 (2–3), 341–364. https://doi.org/10.1007/s00382-008-0441-3.

Ledley, T.S., 1991. Snow on sea ice: competing effects in shaping climate. J. Geophys. Res., Atmos. 96 (D9), 17195–17208. https://doi.org/10.1029/91JD01439.

Lenain, L., Pizzo, N., 2020. The contribution of high-frequency wind-generated surface waves to the Stokes drift. J. Phys. Oceanogr. 50 (12), 3455–3465. https://doi.org/10.1175/JPO-D-20-0116.1.

Li, M., Garrett, C., Skyllingstad, E., 2005. A regime diagram for classifying turbulent large eddies in the upper ocean. Deep-Sea Res., Part 1, Oceanogr. Res. Pap. 52, 259–278. https://doi.org/10.1016/j.dsr.2004.09.004.

Li, Q., Fox-Kemper, B., 2017. Assessing the effects of Langmuir turbulence on the entrainment buoyancy flux in the ocean surface boundary layer. J. Phys. Oceanogr. 47, 2863–2886. https://doi.org/10.1175/JPO-D-17-0085.1.

Li, Q., Fox-Kemper, B., 2020. Anisotropy of Langmuir turbulence and the Langmuir-enhanced mixed layer entrainment. Phys. Rev. Fluids 5, 013803. https://doi.org/10.1103/PhysRevFluids.5.013803.

Li, Q., Fox-Kemper, B., Breivik, O., Webb, A., 2017. Statistical models of global Langmuir mixing. Ocean Model. 113, 95–114. https://doi.org/10.1016/j.ocemod.2017.03.016.

Li, Q., Reichl, B.G., Fox-Kemper, B., Adcroft, A.J., Belcher, S., Danabasoglu, G., et al., 2019. Comparing ocean boundary vertical mixing schemes including Langmuir turbulence. J. Adv. Model. Earth Syst. 11 (11), 3545–3592. https://doi.org/10.1029/2019MS001810.

Li, Q., Webb, A., Fox-Kemper, B., Craig, A., Danabasoglu, G., Large, W.G., Vertenstein, M., 2016. Langmuir mixing effects on global climate: WAVE-WATCH III in CESM. Ocean Model. 103, 145–160. https://doi.org/10.1016/j.ocemod.2015.07.020.

Liang, J.-H., Deutsch, C., McWilliams, J.C., Baschek, B., Sullivan, P.P., Chiba, D., 2013. Parameterizing bubble-mediated air-sea gas exchange and its effect on ocean ventilation. Glob. Biogeochem. Cycles 27 (3), 894–905. https://doi.org/10.1002/gbc.20080.

Liang, J.-H., Emerson, S.R., D'Asaro, E.A., McNeil, C.L., Harcourt, R.R., Sullivan, P.P., et al., 2017. On the role of sea-state in bubble-mediated air-sea gas flux during a winter storm. J. Geophys. Res., Oceans 122 (4), 2671–2685. https://doi.org/10.1002/2016JC012408.

Lien, R.-C., D'Asaro, E.A., 2006. Measurement of turbulent kinetic energy dissipation rate with a Lagrangian float. J. Atmos. Ocean. Technol. 23 (7), 964–976. https://doi.org/10.1175/JTECH1890.1.

Lin, X., Xie, S.-P., Chen, X., Xu, L., 2006. A well-mixed warm water column in the central Bohai Sea in summer: effects of tidal and surface wave mixing. J. Geophys. Res., Oceans 111 (C11). https://doi.org/10.1029/2006JC003504.

Liu, W.T., Katsaros, K.B., Businger, J.A., 1979. Bulk parameterization of air-sea exchanges of heat and water vapor including the molecular constraints at the interface. J. Atmos. Sci. 36 (9), 1722–1735. https://doi.org/10.1175/1520-0469(1979)036<1722:BPOASE>2.0.CO;2.

Lund, B., Collins III, C.O., Tamura, H., Graber, H.C., 2016. Multi-directional wave spectra from marine X-band radar. Ocean Dyn. 66, 973–988. https://doi.org/10.1007/s10236-016-0961-z.

MacKinnon, J.A., Nash, J.D., Alford, M.H., Lucas, A.J., Mickett, J.B., Shroyer, E., et al., 2016. A tale of two spicy seas. Oceanography. https://www.jstor.org/stable/24862669.

Mahadevan, A., D'Asaro, E., Lee, C., Perry, M.J., 2012. Eddy-driven stratification initiates North Atlantic spring phytoplankton blooms. Science 337 (6090), 54–58. https://doi.org/10.1126/science.1218740.

Manucharyan, G.E., Thompson, A.F., 2017. Submesoscale sea ice-ocean interactions in marginal ice zones. J. Geophys. Res., Oceans 122 (12), 9455–9475. https://doi.org/10.1002/2017JC012895.

McCaffrey, K., Fox-Kemper, B., Hamlington, P., Thomson, J., 2015. Characterization of turbulence anisotropy, coherence, and intermittency at a prospective tidal energy site: observational data analysis. Renew. Energy 76, 441–453. https://doi.org/10.1016/j.renene.2014.11.063.

McPhee, M.G., 1994. On the turbulent mixing length in the oceanic boundary layer. J. Phys. Oceanogr. 24 (9), 2014–2031. https://doi.org/10.1175/1520-0485(1994)024<2014:OTTMLI>2.0.CO;2.

McPhee, M.G., Martinson, D.G., 1994. Turbulent mixing under drifting pack ice in the Weddell Sea. Science 263 (5144), 218–221. https://doi.org/10.1126/science.263.5144.218.

McPhee, M.G., Stanton, T.P., 1996. Turbulence in the statically unstable oceanic boundary layer under Arctic leads. J. Geophys. Res., Oceans 101 (C3), 6409–6428. https://doi.org/10.1029/95JC03842.

McWilliams, J., Restrepo, J., 1999. The wave-driven ocean circulation. J. Phys. Oceanogr. 29 (10), 2523–2540. https://doi.org/10.1175/1520-0485(1999)029<2523:TWDOC>2.0.CO;2.

McWilliams, J.C., 2016. Submesoscale currents in the ocean. Proc. R. Soc. A 472 (2189), 20160117. https://doi.org/10.1098/rspa.2016.0117.

McWilliams, J.C., Fox-Kemper, B., 2013. Oceanic wave-balanced surface fronts and filaments. J. Fluid Mech. 730, 464–490. https://doi.org/10.1017/jfm.2013.348.

McWilliams, J.C., Gula, J., Molemaker, M.J., Renault, L., Shchepetkin, A.F., 2015. Filament frontogenesis by boundary layer turbulence. J. Phys. Oceanogr. 45 (8), 1988–2005. https://doi.org/10.1175/JPO-D-14-0211.1.

McWilliams, J.C., Huckle, E., Liang, J.-H., Sullivan, P.P., 2012. The wavy Ekman layer: Langmuir circulations, breaking waves, and Reynolds stress. J. Phys. Oceanogr. 42 (11), 1793–1816.

McWilliams, J.C., Sullivan, P.P., 2000. Vertical mixing by Langmuir circulations. Spill Sci. Technol. Bull. 6, 225–237. https://doi.org/10.1016/S1353-2561(01)00041-X.

McWilliams, J.C., Sullivan, P.P., Moeng, C.-H., 1997. Langmuir turbulence in the ocean. J. Fluid Mech. 334, 1–30. https://doi.org/10.1017/S0022112096004375.

Mellor, G.L., Yamada, T., 1982. Development of a turbulence closure model for geophysical fluid problems. Rev. Geophys. 20 (4), 851–875. https://doi.org/10.1029/RG020i004p00851.

Mensa, J.A., Timmermans, M.-L., 2017. Characterizing the seasonal cycle of upper-ocean flows under multi-year sea ice. Ocean Model. 113, 115–130. https://doi.org/10.1016/j.ocemod.2017.03.009.

Min, H.S., Noh, Y., 2004. Influence of the surface heating on Langmuir circulation. J. Phys. Oceanogr. 34 (12), 2630–2641. https://doi.org/10.1175/JPOJPO-2654.1.

Monin, A., Obukhov, A., 1954. Basic laws of turbulent mixing in the surface layer of the atmosphere. Contrib. Geophys. Inst. Acad. Sci. USSR 151 (163), e187.

Monismith, S.G., Cowen, E.A., Nepf, H.M., Magnadaudet, J., Thais, L., 2007. Laboratory observations of mean flows under surface gravity waves. J. Fluid Mech. 573, 131–147. https://doi.org/10.1017/S0022112006003594.

Monterey, G.I., Levitus, S., 1997. Seasonal Variability of Mixed Layer Depth for the World Ocean. US Department of Commerce, National Oceanic and Atmospheric Administration . . . .

Moulin, A.J., Moum, J.N., Shroyer, E.L., 2018. Evolution of turbulence in the Diurnal warm layer. J. Phys. Oceanogr. 48 (2), 383–396. https://doi.org/10.1175/JPO-D-17-0170.1.

Mukherjee, S., Ramachandran, S., Tandon, A., Mahadevan, A., 2016. Production and destruction of eddy kinetic energy in forced submesoscale eddy-resolving simulations. Ocean Model. 105, 44–59. https://doi.org/10.1016/j.ocemod.2016.07.002.

Muñoz-Esparza, D., Sharman, R.D., Lundquist, J.K., 2018. Turbulence dissipation rate in the atmospheric boundary layer: Observations and WRF mesoscale modeling during the XPIA field campaign. Mon. Weather Rev. 146 (1), 351–371. https://doi.org/10.1175/MWR-D-17-0186.1.

Niiler, P., Kraus, E., 1977. One-dimensional models of the upper ocean. In: Kraus, E. (Ed.), Modelling and Prediction of the Upper Layers of the Ocean. Pergamon Press, pp. 143–172.

Nurser, A.G., Griffies, S.M., 2019. Relating the diffusive salt flux just below the ocean surface to boundary freshwater and salt fluxes. J. Phys. Oceanogr. 49 (9), 2365–2376. https://doi.org/10.1175/JPO-D-19-0037.1.

Oakey, N.S., 1982. Determination of the rate of dissipation of turbulent energy from simultaneous temperature and velocity shear microstructure measurements. J. Phys. Oceanogr. 12, 256–271. https://doi.org/10.1175/1520-0485(1982)012<0256:DOTROD>2.0.CO;2.

Oakey, N.S., Elliott, J.A., 1982. Dissipation within the surface mixed layer. J. Phys. Oceanogr. 12, 171–185. https://doi.org/10.1175/1520-0485(1982)012<0171:DWTSML>2.0.CO;2.

O'Donnell, J., Wilson, R.E., Lwiza, K., Whitney, M., Bohlen, W.F., Codiga, D., et al., 2014. The physical oceanography of Long Island Sound. In: Long Island Sound. Springer, pp. 79–158.

Orenstein, P., 2018. Can we predict short term highs and lows in the Indian monsoon? Identifying and evaluating monsoon intraseasonal oscillations in climate data. ScB thesis. Geology-Physics/Mathematics, Brown University. http://www.geo.brown.edu/research/Fox-Kemper/pubs/pdfs/Orenstein18.pdf.

Osborn, T.R., 1980. Estimates of the local rate of vertical diffusion from dissipation measurements. J. Phys. Oceanogr. 10, 83–89. https://doi.org/10.1175/1520-0485(1980)010<0083:EOTLRO>2.0.CO;2.

Otero, J., Wittenberg, R.W., Worthing, R.A., Doering, C.R., 2002. Bounds on Rayleigh–Bénard convection with an imposed heat flux. J. Fluid Mech. 473, 191–199. https://doi.org/10.1017/S0022112002002410.

Pearson, B., Fox-Kemper, B., Bachman, S.D., Bryan, F.O., 2017. Evaluation of scale-aware subgrid mesoscale eddy models in a global eddy-rich model. Ocean Model. 115, 42–58. https://doi.org/10.1016/j.ocemod.2017.05.007.

Pearson, B., Grant, A.L., Polton, J.A., Belcher, S.E., 2015. Langmuir turbulence and surface heating in the ocean surface boundary layer. J. Phys. Oceanogr. 45 (12), 2897–2911. https://doi.org/10.1175/JPO-D-15-0018.1.

Pearson, J., Fox-Kemper, B., Barkan, R., Choi, J., Bracco, A., McWilliams, J.C., 2019. Impacts of Convergence on Structure Functions from Surface Drifters in the Gulf of Mexico. J. Phys. Oceanogr. 49 (3), 675–690. https://doi.org/10.1175/JPO-D-18-0029.1.

Pearson, J., Fox-Kemper, B., Pearson, B., Chang, H., Haus, B.K., Horstmann, J., et al., 2020. Biases in structure functions from observations of submesoscale flows. J. Geophys. Res., Oceans. https://doi.org/10.1029/2019JC015769.

Pham, H.T., Sarkar, S., 2018. Ageostrophic secondary circulation at a submesoscale front and the formation of gravity currents. J. Phys. Oceanogr. 48 (10), 2507–2529. https://doi.org/10.1175/JPO-D-17-0271.1.

Phillips, O., 1961. A note on the turbulence generated by gravity waves. J. Geophys. Res. 66 (9), 2889–2893. https://doi.org/10.1029/JZ066i009p02889.

Pinkel, R., Goldin, M.A., Smith, J.A., Sun, O.M., Aja, A.A., Bui, M.N., Hughen, T., 2011. The wirewalker: A vertically profiling instrument carrier powered by ocean waves. J. Atmos. Ocean. Technol. 28 (3), 426–435. https://doi.org/10.1175/2010JTECHO805.1.

Pollard, R.T., Rhines, P.B., Thompson, R.O.R.Y., 1973. The deepening of the wind-mixed layer. Geophys. Fluid Dyn. 4 (4), 381–404. https://doi.org/10.1080/03091927208236105.

Polton, J.A., Belcher, S.E., 2007. Langmuir turbulence and deeply penetrating jets in an unstratified mixed layer. J. Geophys. Res., Oceans 112 (C9). https://doi.org/10.1029/2007JC004205.

Price, J.F., 1979. On the scaling of stress-driven entrainment experiments. J. Fluid Mech. 90 (3), 509–529. https://doi.org/10.1017/S0022112079002366.

Price, J.F., Weller, R.A., Pinkel, R., 1986. Diurnal cycling: observations and models of the upper ocean response to diurnal heating, cooling, and wind mixing. J. Geophys. Res., Oceans 91, 8411–C7 8427. https://doi.org/10.1029/JC091iC07p08411.

Qiao, F., Song, Z., Bao, Y., Song, Y., Shu, Q., Huang, C., Zhao, W., 2013. Development and evaluation of an Earth System Model with surface gravity waves. J. Geophys. Res., Oceans 118 (9), 4514–4524. https://doi.org/10.1002/jgrc.20327.

Qiao, F., Yuan, Y., Deng, J., Dai, D., Song, Z., 2016. Wave–turbulence interaction-induced vertical mixing and its effects in ocean and climate models. Philos. Trans. R. Soc. A, Math. Phys. Eng. Sci. 374 (2065), 20150201. https://doi.org/10.1098/rsta.2015.0201.

Qiao, F., Yuan, Y., Ezer, T., Xia, C., Yang, Y., Lü, X., Song, Z., 2010. A three-dimensional surface wave–ocean circulation coupled model and its initial testing. Ocean Dyn. 60 (5), 1339–1355. https://doi.org/10.1007/s10236-010-0326-y.

Qiao, F., Yuan, Y., Yang, Y., Zheng, Q., Xia, C., Ma, J., 2004. Wave-induced mixing in the upper ocean: distribution and application to a global ocean circulation model. Geophys. Res. Lett. 31 (11). https://doi.org/10.1029/2004GL019824.

Reffray, G., Bourdalle-Badie, R., Calone, C., 2015. Modelling turbulent vertical mixing sensitivity using a 1-D version of NEMO. Geosci. Model Dev. 8 (1), 69–86. https://doi.org/10.5194/gmd-8-69-2015.

Reichl, B.G., Hallberg, R., 2018. A simplified energetics based Planetary Boundary Layer (ePBL) approach for ocean climate simulations. Ocean Model. 132, 112–129. https://doi.org/10.1016/j.ocemod.2018.10.004.

Reichl, B.G., Wang, D., Hara, T., Ginis, I., Kukulka, T., 2016. Langmuir turbulence parameterization in tropical cyclone conditions. J. Phys. Oceanogr. 46 (3), 863–886. https://doi.org/10.1175/JPO-D-15-0106.1.

Renault, L., McWilliams, J.C., Gula, J., 2018. Dampening of submesoscale currents by air-sea stress coupling in the Californian upwelling system. Sci. Rep. 8 (1), 1–8. https://doi.org/10.1038/s41598-018-31602-3.

Renault, L., Molemaker, M.J., McWilliams, J.C., Shchepetkin, A.F., Lemarié, F., Chelton, D., et al., 2016. Modulation of wind work by oceanic current interaction with the atmosphere. J. Phys. Oceanogr. 46 (6), 1685–1704. https://doi.org/10.1175/JPO-D-15-0232.1.

Roach, L.A., Horvat, C., Dean, S.M., Bitz, C.M., 2018. An emergent sea ice floe size distribution in a global coupled ocean-sea ice model. J. Geophys. Res., Oceans 123 (6), 4322–4337. https://doi.org/10.1029/2017JC013692.

Roemmich, D., Alford, M.H., Claustre, H., Johnson, K.S., King, B., Moum, J., et al., 2019. On the future of Argo: a global, full-depth, multi-disciplinary array. Front. Mar. Sci. 6, 439. https://doi.org/10.3389/fmars.2019.00439.

Rudnick, D.L., Ferrari, R., 1999. Compensation of horizontal temperature and salinity gradients in the ocean mixed layer. Science 283 (5401), 526–529. https://doi.org/10.1126/science.283.5401.526.

Sallée, J.-B., Shuckburgh, E., Bruneau, N., Meijers, A.J.S., Bracegirdle, T.J., Wang, Z., 2013. Assessment of Southern Ocean mixed-layer depths in CMIP5 models: historical bias and forcing response. J. Geophys. Res., Oceans 118 (4), 1845–1862. https://doi.org/10.1002/jgrc.20157.

Samanta, D., Hameed, S.N., Jin, D., Thilakan, V., Ganai, M., Rao, S.A., Deshpande, M., 2018. Impact of a narrow coastal Bay of Bengal sea surface temperature front on an Indian summer monsoon simulation. Sci. Rep. 8 (1), 17694. https://doi.org/10.1038/s41598-018-35735-3.

Sanford, T.B., Price, J.F., Girton, J.B., Webb, D.C., 2007. Highly resolved observations and simulations of the ocean response to a hurricane. Geophys. Res. Lett. 34, 13. https://doi.org/10.1029/2007GL029679.

Shchepetkin, A.F., McWilliams, J.C., 2009. Computational kernel algorithms for fine-scale, multiprocess, longtime oceanic simulations. In: Temam, R.M., Tribbia, J.J. (Eds.), Handbook of Numerical Analysis, Vol. 14. Elsevier, pp. 121–183.

Skyllingstad, E.D., Denbo, D.W., 1995. An ocean large-eddy simulation of Langmuir circulations and convection in the surface mixed layer. J. Geophys. Res., Oceans 100, 8501–8522. https://doi.org/10.1029/94JC03202.

Smith, K.M., Hamlington, P.E., Fox-Kemper, B., 2016. Effects of submesoscale turbulence on ocean tracers. J. Geophys. Res., Oceans 121 (1), 908–933. https://doi.org/10.1002/2015JC011089.

Smith, K.M., Hamlington, P.E., Niemeyer, K.E., Fox-Kemper, B., Lovenduski, N.S., 2018. Effects of Langmuir turbulence on upper ocean carbonate chemistry. J. Adv. Model. Earth Syst. 10. https://doi.org/10.1029/2018MS001486.

Snow, K., Hogg, A.M., Downes, S.M., Sloyan, B.M., Bates, M.L., Griffies, S.M., 2015. Sensitivity of abyssal water masses to overflow parameterisations. Ocean Model. 89, 84–103. https://doi.org/10.1016/j.ocemod.2015.03.004.

Soloviev, A.V., Lukas, R., Donelan, M.A., Haus, B.K., Ginis, I., 2014. The air-sea interface and surface stress under tropical cyclones. Sci. Rep. 4, 5306. https://doi.org/10.1038/srep05306.

Souza, A.N., Wagner, G., Ramadhan, A., Allen, B., Churavy, V., Schloss, J., et al., 2020. Uncertainty quantification of ocean parameterizations: application to the k-profile-parameterization for penetrative convection. J. Adv. Model. Earth Syst., e2020MS002108. https://doi.org/10.1029/2020MS002108.

Stommel, H., 1979. Determination of water mass properties of water pumped down from the Ekman layer to the geostrophic flow below. Proc. Natl. Acad. Sci. 76 (7), 3051–3055. https://doi.org/10.1073/pnas.76.7.3051.

Su, Z., Wang, J., Klein, P., Thompson, A.F., Menemenlis, D., 2018. Ocean submesoscales as a key component of the global heat budget. Nat. Commun. 9 (1), 1–8. https://doi.org/10.1038/s41467-018-02983-w.

Sullivan, P., McWilliams, J., Melville, W., 2004. The oceanic boundary layer driven by wave breaking with stochastic variability. Part 1. Direct numerical simulations. J. Fluid Mech. 507, 143–174. https://doi.org/10.1017/S0022112004008882.

Sullivan, P.P., McWilliams, J.C., 2010. Dynamics of winds and currents coupled to surface waves. Annu. Rev. Fluid Mech. 42, 19–42. https://doi.org/10.1146/annurev-fluid-121108-145541.

Sullivan, P.P., McWilliams, J.C., 2019. Langmuir turbulence and filament frontogenesis in the oceanic surface boundary layer. J. Fluid Mech. 879, 512–553. https://doi.org/10.1017/jfm.2019.655.

Sullivan, P.P., McWilliams, J.C., Moeng, C.H., 1994. A subgrid-scale model for Large-Eddy Simulation of planetary boundary-layer flows. Bound.-Layer Meteorol. 71 (3), 247–276. https://doi.org/10.1007/BF00713741.

Sullivan, P.P., McWilliams, J.C., Patton, E.G., 2014. Large-eddy simulation of marine atmospheric boundary layers above a spectrum of moving waves. J. Atmos. Sci. 71 (11), 4001–4027. https://doi.org/10.1175/JAS-D-14-0095.1.

Sullivan, P.P., McWilliams, J.C., Weil, J.C., Patton, E.G., Fernando, H.J.S., 2020. Marine boundary layers above heterogeneous SST: Across-front winds. J. Atmos. Sci. 77 (12), 4251–4275. https://doi.org/10.1175/JAS-D-20-0062.1.

Sullivan, P.P., Romero, L., McWilliams, J.C., Melville, W.K., 2012. Transient evolution of Langmuir turbulence in ocean boundary layers driven by hurricane winds and waves. J. Phys. Oceanogr. 42 (11), 1959–1980. https://doi.org/10.1175/JPO-D-12-025.1.

Sutherland, G., Christensen, K., Ward, B., 2014. Evaluating Langmuir turbulence parameterizations in the ocean surface boundary layer. J. Geophys. Res., Oceans 119 (3), 1899–1910. https://doi.org/10.1002/2013JC009537.

Sutherland, G., Ward, B., Christensen, K., 2013. Wave-turbulence scaling in the ocean mixed layer. Ocean. Sci. 9 (4), 597–608. https://doi.org/10.5194/os-9-597-2013.

Suzuki, N., Fox-Kemper, B., 2016. Understanding Stokes forces in the wave-averaged equations. J. Geophys. Res., Oceans 121, 1–18. https://doi.org/10.1002/2015JC011566.

Suzuki, N., Fox-Kemper, B., Hamlington, P.E., Van Roekel, L.P., 2016. Surface waves affect frontogenesis. J. Geophys. Res., Oceans 121, 1–28. https://doi.org/10.1002/2015JC011563.

Suzuki, N., Hara, T., Sullivan, P.P., 2011. Turbulent airflow at young sea states with frequent wave breaking events: large-eddy simulation. J. Atmos. Sci. 68 (6), 1290–1305. https://doi.org/10.1175/2011JAS3619.1.

Sverdrup, H., 1953. On conditions for the vernal blooming of phytoplankton. ICES J. Mar. Sci. 18 (3), 287–295.

Taylor, J.R., 2018. Accumulation and subduction of buoyant material at submesoscale fronts. J. Phys. Oceanogr. 48 (6), 1233–1241. https://doi.org/10.1175/JPO-D-17-0269.1.

Taylor, J.R., Ferrari, R., 2011. Shutdown of turbulent convection as a new criterion for the onset of spring phytoplankton blooms. Limnol. Oceanogr. 56 (6), 2293–2307. https://doi.org/10.4319/lo.2011.56.6.2293.

Taylor, J.R., Smith, K.M., Vreugdenhil, C.A., 2020. The influence of submesoscales and vertical mixing on the export of sinking tracers in large-eddy simulations. J. Phys. Oceanogr. 50 (5), 1319–1339. https://doi.org/10.1175/JPO-D-19-0267.1.

Teixeira, M., Belcher, S., 2002. On the distortion of turbulence by a progressive surface wave. J. Fluid Mech. 458, 229–267. https://doi.org/10.1017/S0022112002007838.

Thomas, L.N., Tandon, A., Mahadevan, A., 2008. Submesoscale processes and dynamics. In: Ocean Modeling in an Eddying Regime, Vol. 177, pp. 17–38.

Thomas, L.N., Taylor, J.R., Ferrari, R., Joyce, T.M., 2013. Symmetric instability in the Gulf Stream. Deep-Sea Res., Part 2, Top. Stud. Oceanogr. 91, 96–110. https://doi.org/10.1016/j.dsr2.2013.02.025.

Thomson, J., 2012. Wave breaking dissipation observed with "SWIFT" drifters. J. Atmos. Ocean. Technol. 29 (12), 1866–1882. https://doi.org/10.1175/JTECH-D-12-00018.1.

Thomson, J., Polagye, B., Durgesh, V., Richmond, M.C., 2012. Measurements of turbulence at two tidal energy sites in Puget Sound, WA. IEEE J. Ocean. Eng. 37 (3), 363–374. https://doi.org/10.1109/JOE.2012.2191656.

Thorpe, S., Osborn, T., Jackson, J., Hall, A., Lueck, R., 2003. Measurements of turbulence in the upper-ocean mixing layer using autosub. J. Phys. Oceanogr. 33 (1), 122–145. https://doi.org/10.1175/1520-0485(2003)033<0122:MOTITU>2.0.CO;2.

Thorpe, S.A., 2007. An Introduction to Ocean Turbulence. Cambridge University Press, Cambridge.

Torma, P., Krámer, T., 2017. Modeling the effect of waves on the diurnal temperature stratification of a shallow lake. Period. Polytech., Civil Eng. 61 (2), 165–175. https://doi.org/10.3311/PPci.8883.

Troehn, I., Mahrt, L., 1986. A simple model of the atmospheric boundary layer; sensitivity to surface evaporation. Bound.-Layer Meteorol. 37, 129–148. https://doi.org/10.1007/BF00122760.

Tsujino, H., Urakawa, L.S., Griffies, S.M., Danabasoglu, G., Adcroft, A.J., Amaral, A.E., et al., 2020. Evaluation of global ocean–sea-ice model simulations based on the experimental protocols of the Ocean Model Intercomparison Project phase 2 (OMIP-2). Geosci. Model Dev. 13, 3643–3708. https://doi.org/10.5194/gmd-13-3643-2020.

Umlauf, L., Burchard, H., 2005. Second-order turbulence closure models for geophysical boundary layers. A review of recent work. Cont. Shelf Res. 25, 795–827. https://doi.org/10.1016/j.csr.2004.08.004.

Umlauf, L., Burchard, H., Bolding, K., 2016. GOTM sourcecode and test case documentation. Tech. Rep.. Leibniz Institute for Baltic Sea Research. http://gotm.net.

Van Roekel, L., Adcroft, A.J., Danabasoglu, G., Griffies, S.M., Kauffman, B., Large, W., et al., 2018. The KPP boundary layer scheme for the ocean: revisiting its formulation and benchmarking one-dimensional simulations relative to LES. J. Adv. Model. Earth Syst. 10 (11), 2647–2685. https://doi.org/10.1029/2018MS001336.

Van Roekel, L.P., Fox-Kemper, B., Sullivan, P.P., Hamlington, P.E., Haney, S.R., 2012. The form and orientation of Langmuir cells for misaligned winds and waves. J. Geophys. Res., Oceans 117, C05001. https://doi.org/10.1029/2011JC007516.

van Sebille, E., Aliani, S., Law, K.L., Maximenko, N., Alsina, J.M., Bagaev, A., et al., 2020. The physical oceanography of the transport of floating marine debris. Environ. Res. Lett. 15. https://doi.org/10.1088/1748-9326/ab6d7d.

Vieira, M., Guimaraes, P.V., Violante-Carvalho, N., Benetazzo, A., Bergamasco, F., Pereira, H., 2020. A low-cost stereo video system for measuring directional wind waves. J. Mar. Sci. Eng. 8 (11), 831. https://doi.org/10.3390/jmse8110831.

Von Kármán, T., 1930. Mechanische änlichkeit und turbulenz. Nachr. Ges. Wiss. Gött., Math.-Phys. Kl. 1930, 58–76.

Wang, D., Kukulka, T., Reichl, B.G., Hara, T., Ginis, I., 2019a. Wind–wave misalignment effects on Langmuir turbulence in tropical cyclone conditions. J. Phys. Oceanogr. 49 (12), 3109–3126. https://doi.org/10.1175/JPO-D-19-0093.1.

Wang, P., Ozgokmen, T.M., 2018. Langmuir circulation with explicit surface waves from moving-mesh modeling. Geophys. Res. Lett. 45 (1), 216–226. https://doi.org/10.1002/2017GL076009.

Wang, S., Wang, Q., Shu, Q., Scholz, P., Lohmann, G., Qiao, F., 2019b. Improving the upper-ocean temperature in an ocean climate model (FESOM 1.4): Shortwave penetration versus mixing induced by nonbreaking surface waves. J. Adv. Model. Earth Syst. 11 (2), 545–557. https://doi.org/10.1029/2018MS001494.

Ward, B., Wanninkhof, R., Minnett, P.J., Head, M.J., 2004. SkinDeEP: a profiling instrument for upper-decameter sea surface measurements. J. Atmos. Ocean. Technol. 21 (2), 207–222. https://doi.org/10.1175/1520-0426(2004)021<0207:SAPIFU>2.0.CO;2.

Waterhouse, A.F., MacKinnon, J.A., Nash, J.D., Alford, M.H., Kunze, E., Simmons, H.L., et al., 2014. Global patterns of diapycnal mixing from measurements of the turbulent dissipation rate. J. Phys. Oceanogr. 44 (7), 1854–1872. https://doi.org/10.1175/JPO-D-13-0104.1.

Webb, A., Fox-Kemper, B., 2011. Wave spectral moments and Stokes drift estimation. Ocean Model. 40 (3–4), 273–288. https://doi.org/10.1016/j.ocemod.2011.08.007.

Webb, A., Fox-Kemper, B., 2015. Impacts of wave spreading and multidirectional waves on estimating Stokes drift. Ocean Model. 96 (1), 49–64. https://doi.org/10.1016/j.ocemod.2014.12.007.

Weller, R.A., Price, J., 1988. Langmuir circulation within the oceanic mixed layer. Deep-Sea Res., A, Oceanogr. Res. Pap. 35, 711–747. https://doi.org/10.1016/0198-0149(88)90027-1.

Winton, M., Takahashi, K., Held, I.M., 2010. Importance of ocean heat uptake efficacy to transient climate change. J. Climate 23 (9), 2333–2344. https://doi.org/10.1175/2009JCLI3139.1.

Wu, L., Rutgersson, A., Sahlée, E., 2015. Upper-ocean mixing due to surface gravity waves. J. Geophys. Res., Oceans 120 (12), 8210–8228. https://doi.org/10.1002/2015JC011329.

Wyngaard, J.C., 2010. Turbulence in the Atmosphere. Cambridge University Press.

Xuan, A., Deng, B.-Q., Shen, L., 2019. Study of wave effect on vorticity in Langmuir turbulence using wave-phase-resolved large-eddy simulation. J. Fluid Mech. 875, 175–224. https://doi.org/10.1017/jfm.2019.481.

Yankovsky, E., Legg, S., Hallberg, R.W., 2021. Parameterization of submesoscale symmetric instability in dense flows along topography. J. Adv. Model. Earth Syst. 13 (6), e2020MS002049. https://doi.org/10.1029/2020MS002049.

Zhao, B., Qiao, F., Cavaleri, L., Wang, G., Bertotti, L., Liu, L., 2017. Sensitivity of typhoon modeling to surface waves and rainfall. J. Geophys. Res., Oceans 122, 2017–2028. https://doi.org/10.1002/2016JC012262.

Zheng, Z., Harcourt, R.R., D'Asaro, E.A., 2021. Evaluating Monin-Obukhov scaling in the unstable oceanic surface layer. J. Phys. Oceanogr. 51 (3), 911–930. https://doi.org/10.1175/JPO-D-20-0201.1.